

Solar Energy

Enhancing the filling of perovskite material in the scaffold layer to improve the conversion efficiency of printable perovskite solar cells

--Manuscript Draft--

Manuscript Number:	SEJ-D-25-00611R1
Article Type:	Research paper
Section/Category:	Photovoltaic Cells and Cell Physics
Keywords:	Printed mesoscopic perovskite solar cells; Filling dynamics; Infiltration; crystallization
Abstract:	<p>The complete filling of perovskite materials into mesoporous TiO₂/ZrO₂ scaffold film remains a great challenge for achieving a high conversion efficiency in printed mesoscopic perovskite solar cells. However, there is a lack of a precise understanding of the filling dynamics to guide the optimization process. In this study, a process comprising the beginning infiltration step and the subsequent crystallization step have been proposed to optimize filling behavior. By introducing macropores in the first step using the polystyrene microsphere templating method to facilitate the infiltration of the perovskite precursor solution, combined with the bottom-up controlled crystallization assisted by a low-pressure gas pumping method in the second step, the perovskite material is more completely filled into the TiO₂/ZrO₂ scaffold layer. The photovoltaic performance of the perovskite solar cell shows that the conversion efficiency is improved by 375% compared to the weakly filled solar cells. This work contributes to enhance the filling of perovskite material and improve the conversion efficiency of printable perovskite solar cells.</p>

Responses to Editor' Comments

If you wish to address the reviewers' comments, please submit a revised manuscript addressing all the reviewers' comments. Along with your revised manuscript, please submit the following:

1. Detailed point-by-point response to each reviewer's comment with clear identification of the page number in the revised manuscript where the change has been made. Please note that you are not having a dialog with the reviewer. You need to address each comment at appropriate locations in the revised manuscript for a potential reader with the same question. Please follow the example in <https://tinyurl.com/reviewer-responses>

Reply: Thank you for your comment. A point-by-point response has been prepared. All the revisions can be easily located by page numbers.

2. Marked manuscript highlighting the changes made and including marginal annotations next to each change, identifying the reviewer number and the comment number corresponding to the change. Please note that a track-changed document is not sufficient. Please follow the example in <https://tinyurl.com/marked-manuscript>

Reply: Thank you for your comment. The changes have been highlighted in the manuscript and the marginal annotations have been added next to the changes.

3. Unmarked clean version of your revised manuscript. Please DO NOT include the original manuscript with your revised submission.

Reply: Thank you for your comment. The unmarked clean version of the revised manuscript has been uploaded.

Please make sure that your revised submission PDF file is assembled exactly in the following order:

1. Responses to Reviewers' Comments
2. Marked manuscript
3. Highlights
4. Unmarked manuscript
5. Tables
6. Figures
7. Supplementary material, if any (optional)

8. Other files, if any (DO NOT INCLUDE ORIGINAL SUBMISSION)

Reply: Thank you for your comment. Following your suggestions.

I sincerely hope that my replies address your concerns satisfactorily, and I would greatly appreciate your continued guidance toward the successful publication of this work.

Responses to Reviewers' Comments – Reviewer #1

Review comments for "Enhancing the filling of perovskite material in the scaffold layer to improve the conversion efficiency of printable perovskite solar cells." The authors have studied perovskite-based solar cells, mainly focusing on the fabrication of devices using industrially viable printing technology. This is a very interesting and much-needed contribution to current energy demands. The manuscript is well-organized and well-written. However, I would like to ask a few questions to clarify certain points.

Reply: Thank the reviewer for your recognition about the novelty and contribution of this paper.

Comments 1: What is the status of adhesion of the perovskite to the scaffold due to increased porosity?

Reply: Thank the reviewer for your comment. In this study, we investigated the infiltration behavior of the perovskite precursor solution into the mesoporous scaffold, without focusing extensively on the adhesion ability of the solidified perovskite material to the scaffold layer. However, based on empirical knowledge, it can be reasonably speculated that a moderate increase in porosity facilitates the infiltration of the perovskite precursor solution, increases the contact area, and subsequently enhances the adhesion of the perovskite material to the mesoporous scaffold through improved mechanical interlocking.

Comments 2: Is there a limit to how much porosity can be introduced before it hinders perovskite?

Reply: Thank the reviewer for your comment. When the porosity of the scaffold film becomes too high, it can lead to structural collapse of the scaffold film itself. Externally, this manifests as delamination, flaking, or powdering of the scaffold layer. This is the main reason why excessive porosity in the scaffold should be avoided. It is important to note that the increased porosity of the scaffold does not inherently cause any damage to the perovskite material.

Comments 3 (Page 6): Change the statement "Finally, the PSCs were annealed at 120°C for 10 min. All the above processes were carried out at a low temperature of 2-3°C" to "All the above processes were carried out at a low temperature of 2-3°C. Finally, the PSCs were annealed at 120°C for 10 min".

Reply: Thank the reviewer for your carefully reading our manuscript. We have revised it as you can see in P6 highlighted with red colour.

Comments 4: How consistent were the performance improvements across multiple device batches?

Reply: Thank you for your comment. Fig. 7 shows the test results of enhanced-filling PSCs from three batches. Compared with the unenhanced-filling PSC in Fig.6, the improvement in conversion efficiency of the enhanced-filling PSCs ranges from 169% to 375%. In all, the enhanced-filling PSCs consistently exhibit improved efficiency.

Comments 5 (Page 16): What is the stability status? Calculate the efficiency based on stability.

Reply: Thank you for your comment. The stability performance of the three parallel enhanced-filling PSCs have been added as Figure S8 in the supporting information. It can be seen that the unencapsulated cells exhibit minimal performance degradation after being exposed to the ambient environment for 15 days.

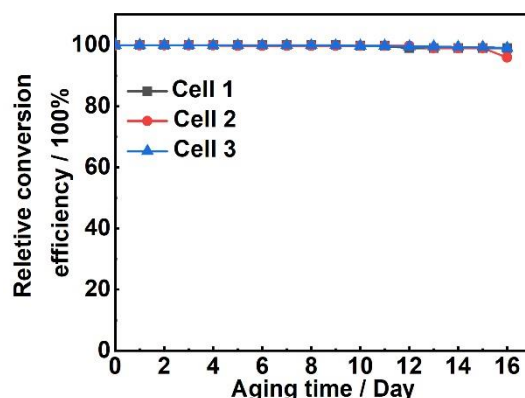


Figure S8 The stability performance of the three parallel En-PSCs

Comments 6: Why is efficiency only 10%? Give the possible reasons.

Reply: Thank you for your comment. Carbon electrodes were employed in this study. Their relatively poor performance in extracting charge carriers at the interface and transporting them through the bulk, compared to metal electrodes, is likely the primary obstacle to further enhancements in device efficiency.

Comments 7 (Page 6): Add device dimensions and the thickness of each layer.

Reply: Thank you for your comment. The detailed information has been added in P6. For current density-voltage (*J-V*) characteristics, the cell has an area of $1 \times 1 \text{ cm}^2$, with a $\text{TiO}_2/\text{ZrO}_2$ scaffold layer thickness of $4 \pm 0.5 \text{ }\mu\text{m}$ and a carbon electrode thickness of $15 \pm 1 \text{ }\mu\text{m}$.

Comments 8 (Page 17): Add future possible ways to improve the performance?

Reply: Thank you for your comment. In the future, enhancing capillary attraction and reducing evaporation will both contribute to the complete filling of perovskite materials into the scaffold film, which as been added at P17 of the manuscript.

Suggestions:

1. All the terms and abbreviations should be introduced in their first appearance.

Reply: Thank the reviewer for your carefully reading our manuscript. We have revised the manuscript and checked it twice. All the revised area has been marked in red and highlighted in yellow.

2. Once again, check grammar and units throughout the manuscript.

Reply: Thank the reviewer for your carefully reading our manuscript. We have checked them. All the revised area has been marked in red and highlighted in yellow.

I sincerely hope that my replies address your concerns satisfactorily, and I would greatly appreciate your continued guidance toward the successful publication of this work.

Responses to Reviewers' Comments – Reviewer #3

Recommendation: Minor revisions

The work addresses a highly relevant topic—perovskite solar cells. Specifically, the authors investigate one of the technological stages in the fabrication of such structures and attempt to identify conditions for optimizing the infiltration of the scaffold layer with perovskite material. The study is engaging and presents results with potential practical applications, although some aspects remain unclear.

Reply: Thank the reviewer for your recognition about the novelty and contribution of this paper.

Several concerns arise:

Comments 1: Why does a portion of the film remain filled when $V_1 > V_2$ (Fig. 3a)? Could the material have simply evaporated?

The claim of having developed a physical model of filling dynamics seems somewhat overstated. At a minimum, basic mathematical expressions describing the relevant processes are necessary.

Reply: Thank you for your comment. During the infiltration process, the solvent evaporates while the solute—namely, the perovskite material—is retained within the scaffold layer. Since complete evaporation of the solvent requires some time, a portion of the perovskite material remains deposited on the upper area of the scaffold layer.

The establishment of basic mathematical models requires specific physical parameters of the perovskite precursor solution and the scaffold system. However, acquiring accurate values is a complex and time-consuming process. We have previously attempted to perform simulations using Fluent, and the results are currently under discussion.

Comments 2: Why is the interface between TiO_2 and ZrO_2 not considered as a possible nucleation site?

Reply: Thank the reviewer for your comments. As the perovskite precursor solution fully infiltrates the scaffold film, nucleation preferentially occurs at the upper and bottom area of the scaffold film under the combined influence of temperature and concentration gradients, without the need for external intervention. When external regulation is applied, nucleation can occur at any location within the scaffold where supersaturation conditions are met, including the $\text{TiO}_2/\text{ZrO}_2$ interface.

However, it is important to note that this interface is not a thermodynamically or kinetically favored site for nucleation.

Comments 3: The study mentions the formation of a temperature gradient and favorable conditions for top-down crystallization due to the cooling of the upper layers caused by evaporation. Could the authors estimate the temperature difference between the upper and lower parts or layer?

Reply: Thank the reviewer for your comments. The solvent used in the perovskite precursor solution is N,N-dimethylformamide (DMF). The evaporation of DMF is an endothermic process, which leads to the formation of a temperature gradient within the scaffold, with the temperature gradually increasing from the upper area to the bottom area.

The enthalpy of vaporization, specific heat capacity, and molecular weight of DMF can be obtained from thermodynamic handbooks, as summarized below.

$$\Delta H_{\text{vap}} \approx 52.3 \text{ kJ/mol (at } 153^\circ\text{C)}; C \approx 2.47 \times 10^{-3} \text{ KJ/g}\cdot\text{K}; M=73.09 \text{ g/mol}$$

Assume that the heat required for DMF evaporation is entirely supplied by the adjacent DMF layer of equal thickness. Then, how much would the temperature of this adjacent DMF layer decrease during the evaporation process?

$$\Delta T = \frac{\Delta H_{\text{vap}}}{CM} \approx 289.7^\circ\text{C}$$

This estimation is intended only for preliminary evaluation and may involve a range of uncertainty; hence, it was not included in the manuscript or cited as a reference.

Comments 4: Why do the quantities of Pb and I differ significantly in Fig. 5b (e.g., near points 4 and 5, by a factor of three), whereas in Fig. 1 they appear nearly identical? Both figures are supposed to represent the same material, MAPbI₃.

Reply: Thank the reviewer for your comments. As shown in Fig. 1, the MAPbI₃ material was barely infiltrated into the scaffold; therefore, the EDS line scan signals for both Pb and I are nearly undetectable throughout the depth. In contrast, in Fig. 5, the infiltration of MAPbI₃ into the scaffold was significantly improved from upper area to bottom area. Given that the relative atomic mass of Pb is approximately twice that of I, and the stoichiometry of MAPbI₃ contains three times more I atoms than Pb atoms, the mass percentage of I is accordingly higher than that of Pb in the EDS results. This is consistent with the observed elemental distribution.

Comments 5: The layer thickness in Fig. 1a is 8 μm , while in Fig. 5a it is less than 4 μm . If the solar cells were fabricated using layers of different thicknesses, the conclusions regarding the effect of porosity cannot be considered well-founded.

Reply: Thank the reviewer for your valuable comments. In Fig. 1 and Figure S2, the scaffold film thickness was reduced from 8 μm to 4 μm , yet the perovskite still failed to infiltrate the scaffold. This indicates that the infiltration is not dependent on the film thickness, but rather on the penetration behavior of the perovskite precursor solution and the crystallization of the solute. During the later stage of cell fabrication, all solar cells were assembled using scaffolds with a thickness of $4 \pm 0.5 \mu\text{m}$. This clarification has been added to Page 6 with red color.

Comments 6 (Page 16): What exactly is meant by the statement about "enhanced structure stability"? If this refers to the reproducibility of parameters across different samples, data for scaffold films without enhanced filling should also be provided.

Reply: Thank you to the reviewer for the comments. This indeed refers to the reproducibility of parameters across different samples. As a comparison, we assembled the same number of Un-En PSCs, among which only 9 exhibited measurable conversion efficiency. The performance data of these efficient devices are presented in Figure S9. Due to the better filling state, the En PSCs generally show higher efficiency. In contrast, the poor filling state in the Un-En PSCs fails to provide stable pathways for charge transport, resulting in only a portion of the cells exhibiting low efficiency.

Comments 7 (Page 14): The criteria for selecting the optimal number of microspheres (degree of porosity) remain unclear. Likewise, it is unclear why a porosity of 30% is said to result in "excessively small" distances between PS microspheres. The center-to-center distance between spheres should still be at least three times their diameter.

Reply: Thank the reviewer for your comments. when PS microspheres occupy 30% of the cross-sectional model area, the number of PS microspheres can be calculated as: Number of PS microspheres = $\frac{1000 \times 2400}{\pi \times 150 \times 150} \approx 34$, where the $1000 \times 2400 \text{ nm}^2$ represents that the area of the 30% $\text{TiO}_2/\text{ZrO}_2$ scaffold layer, and the $\pi \times 150 \times 150 \text{ nm}^2$ represents the area of a PS microspheres.

The average distance between PSs is about 836 nm, and it seems larger than the diameter of the PS (300 nm). However, when the two parameters are of the same order of magnitude, it results in insufficient bonding between particles within the printed scaffold layer, causing problems such as powder detachment and delamination during processing. Based on these experimental observations,

we chose a content of 25% to ensure structural stability. The detailed explanation has been added in the manuscript at P14.

I sincerely hope that my replies address your concerns satisfactorily, and I would greatly appreciate your continued guidance toward the successful publication of this work.

Enhancing the filling of perovskite material in the scaffold layer to improve the conversion efficiency of printable perovskite solar cells

Weiwu Dang¹, Li Liu², Jianhua Chen², Xian Gu², Xuhao Wang², Xiaolan Li²,

Yan Li^{2, *}

¹College of Intelligent Manufacturing, Shaanxi Institute of Technology, Xi'an, Shaanxi 710300, China

²College of New Energy, Xi'an Shiyou University, Xi'an, Shaanxi 710065, China

* Correspondence to: Doc. Yan Li, College of New Energy, Xi'an Shiyou University, Xi'an, Shaanxi 710065, China

E-mail address: li1988yan@163.com

Abstract: The complete filling of perovskite materials into mesoporous TiO₂/ZrO₂ scaffold film remains a great challenge for achieving a high conversion efficiency in printed mesoscopic perovskite solar cells. However, there is a lack of a precise understanding of the filling dynamics to guide the optimization process. In this study, a process comprising the beginning infiltration step and the subsequent crystallization step have been proposed to optimize filling behavior. By introducing macropores in the first step using the polystyrene microsphere templating method to facilitate the infiltration of the perovskite precursor solution, combined with the bottom-up controlled crystallization assisted by a low-pressure gas pumping method in the second step, the perovskite material is more completely filled into the TiO₂/ZrO₂ scaffold layer. The photovoltaic performance of the perovskite solar cell shows that the conversion efficiency is improved by 375% compared to the weakly filled solar cells. This work contributes to enhance the filling of perovskite

material and improve the conversion efficiency of printable perovskite solar cells.

Keywords: Printed mesoscopic perovskite solar cells; Filling dynamics; Infiltration; Crystallization

1. Introduction

The commercial-scale production of perovskite solar cells (PSCs) has attracted widespread attention^{1,2}. The printed mesoscopic PSCs with an all-mesoporous structure can be directly fabricated in the air using a screen printing technique³⁻⁵, which is a promising candidate for the commercialization of solar cells. Years ago, when Han's group⁶ introduced $(5\text{-AVA})_x\text{CH}_3\text{NH}_3(1-x)\text{PbI}_3$ as the light-absorbing material, achieving a conversion efficiency of 10.4% in solar cells with an active cell area of 49 cm². Furthermore, it has been reported that the printed mesoscopic PSCs can keep their initial efficiency unchanged during 1000 hours of light exposure, and these solar cells exhibit long-term stability, lasting over one year in the dark due to the hydrophobic nature of carbon electrodes⁶. Studies also indicate that these solar cells retain more than 97% of their initial efficiency after 2,136 hours under outdoor conditions⁷, and the printable PSCs have passed the widely recognized international standard IEC61215:2016⁸. Nowadays, Wonder Solar Ltd. demonstrates a 110 m² fully printable mesoscopic PSCs outdoor power generation system⁹. Researchers believe that printable mesoscopic PSCs are strong contenders for the commercialization of perovskite solar cells.^{10,11}

In the printed mesoscopic PSCs, removing the hole transport material and replacing the silver/gold electrode with a carbon electrode can reduce the cost of the solar cells and simplify the fabrication process¹²⁻¹⁵. However, preparation of the carbon electrode requires a high-temperature treatment at 400°C, which is higher than the decomposition temperature of the perovskite materials. Therefore, in the solar cell assembly process, the carbon electrode is first deposited onto the TiO₂/ZrO₂ scaffold layer, after which the perovskite, serving as the light-absorbing material, is infiltrated into the scaffold film using a solution-based method¹⁶⁻¹⁸. However, the extent to which perovskite fills the scaffold film is crucial for the performance and stability of the fully printable PSCs¹⁹⁻²¹. A completely filling and good connectivity of the perovskite material in the scaffold film enhances its ability to capture photonic energy, dissociating excitons via the MAPbI₃/TiO₂ heterojunction, and transport holes to carbon electrode, whereas insufficient filling of the perovskite material in the TiO₂/ZrO₂ scaffold film leads to poor light absorption, discontinuous carrier transport channels, and severe internal recombination^{22,23}.

The filling amount of perovskite material is influenced by multiple factors, such as the uncontrolled crystallization of the precursor solution²⁴, the pore structure of the mesoporous scaffold layer^{25,26}, the filling process²⁷ and the interfacial contact between the perovskite and the mesoporous scaffold layer^{28,29}. Many researchers have attempted to manipulate the perovskite precursor, such as Chen et al.³⁰ systematically investigated the impact of various solvents on the filling behavior, and achieved a conversion efficiency of 13.89% by optimizing the ratio of **N,N-dimethylformamide (C₃H₇NO,**

DMF) and dimethyl sulfoxide (C_2H_6OS , DMSO). This optimization improved the wettability and stabilized the mesophase of the perovskite precursor, thereby regulating the crystallization rate of perovskite crystals. Rong et al.³¹ utilized pure DMSO as a solvent due to its strong coordination ability and the formation of a stable intermediate phase (PbI_2 -DMSO- CH_3NH_3I) to dissolve perovskite. This approach effectively inhibited the rapid binding of PbI_2 and CH_3NH_3I while accelerating the infiltration of the perovskite precursor into the scaffold layer. In addition to the manipulation of the solvent, previous results have demonstrated that both pore blockage caused by preferential perovskite crystallization and solvent retention can lead to incomplete filling of the scaffold film³². Bogachuk et al.³³ introduced a sacrificial Polystyrene nanoparticles film into the scaffold film to create nano-cavities enabling the growth of larger perovskite crystals inside the oxide scaffold. However, achieving complete filling of perovskite materials into the TiO_2/ZrO_2 scaffold film is still a great challenge. To reach a fully filled state, a precise understanding of the physical dynamics involved is still required. Moreover, the correlation between solution infiltration and precursor crystallization has yet to be fully established, and the corresponding regulatory mechanisms governing these processes remain unexplored.

In the study, based on the observed filling behavior of $CH_3NH_3PbI_3$ ($MAPbI_3$) into the TiO_2/ZrO_2 scaffold film, the physical filling dynamics were analyzed. The correlation between infiltration and crystallization in enhancing the perovskite materials filling was established. To optimize this process, sub-macropores were introduced into the scaffold layer using the Polystyrene microsphere templating method,

and followed by bottom-up controlled crystallization facilitated by a low-pressure gas pumping method. At last, the photovoltaic performance of the PSCs was evaluated.

2. Experimental

2.1 Materials

Zirconium oxide (ZrO_2) powder and titanium dioxide (TiO_2) powder were purchased from Degussa AG (Germany). N-butanol ($\text{C}_4\text{H}_{10}\text{O}$), terpineol ($\text{C}_{10}\text{H}_{18}\text{O}$), ethyl cellulose ($((\text{C}_{12}\text{H}_{22}\text{O}_5)_n)$) and acetone ($\text{C}_3\text{H}_6\text{O}$) were purchased from Shanghai Reagent Chemical Co., Ltd (China). Lead iodide (PbI_2), methylamine iodide ($\text{CH}_3\text{NH}_3\text{I}$, MAI), DMF, TiO_2 compact layer precursor solution and Carbon electrode material were purchased from Xi'an Yuri Solar Co., Ltd (China). The transparent fluorine-doped tin oxide (FTO, TEC-15, $25 \times 25 \text{ mm}^2$, LOF) conductive glass was used as substrates. The polystyrene (PS) microspheres of $\sim 300 \text{ nm}$ were purchased from Rigor Science Co., Ltd (China).

2.2 Preparation of the TiO_2 and ZrO_2 slurry

For the ZrO_2 slurry, firstly, 0.45 g of ethyl cellulose and 0.6 ml terpineol was dissolved into 5 ml of n-butanol to prepare an ethyl cellulose solution, and 2.5 g of ZrO_2 was dispersed in n-butanol to form a 35 wt% suspension. Secondly, the ethyl cellulose solution and ZrO_2 suspension were mixed by magnetic stirring for 12 h, followed by grinding for 20 min to obtain a ZrO_2 slurry. In order to increase the porosity of the ZrO_2 film by 25%, 0.16 g of PS microspheres was added in the second step.

For the TiO_2 slurry, except that 1.5 g of TiO_2 was dispersed in n-butanol to form a 20 wt% suspension in the first step, the other steps follow the same preparation process

as ZrO₂ slurry. In order to increase the porosity of the TiO₂ film by 25%, 0.07 g of PS microspheres was added in the second step.

2.3 Filling the perovskite into the scaffold film and fabrication of the PSCs

The FTO was cleaned successively in deionized water and alcohol, and dried with N₂ flow. A compact TiO₂ layer was deposited on the etched FTO substrate via spin coating and then annealed at 120°C for 15 min. Subsequently, the TiO₂ films and ZrO₂ films were deposited using screen-printing technique, and then annealed in a tube furnace at 400°C for 30 min to produce the TiO₂/ZrO₂ scaffold films. Then, the carbon film was also deposited using screen-printing technique, and annealed in a tube furnace at 450°C for 30 min.

The MAPbI₃ precursor solution was prepared by dissolving PbI₂ and CH₃NH₃I in DMF at a concentration of 460 mg·mL⁻¹, which was infiltrated from the carbon side, and subsequently spin-coated at 3000 rpm for 10 s. To keep the bottom-up crystallization of the perovskite material, the sample was transferred to the low-pressure chamber of the low-pressure gas pumping equipment³⁴⁻³⁶ and dried at 1000 Pa for 10 min. All the above processes were carried out at a low temperature of 2-3°C. Finally,

the PSCs were annealed at 120°C for 10 min. For current density-voltage (*J-V*) characteristics, the cell has an area of 1 × 1 cm², with a TiO₂/ZrO₂ scaffold layer thickness of 4 ± 0.5 μm and a carbon electrode thickness of 15 ± 1 μm.

Rev.1
Com.3

Rev.1
Com.7

2.4 Characterization

The phase structures of the TiO₂ and ZrO₂ films were measured by an X-ray diffractometer using Cu K_α radiation (XRD, Bruker-D8 ADVANCE, Germany). The

morphology of the scaffold film was characterized using a scanning electron microscope (SEM, ZEISS Sigma 300, Germany). To quantitatively analyze the elemental distribution in perovskite, energy-dispersive X-ray spectroscopy (EDS, Oxford Xplore 30, United Kingdom) was employed. The J - V characteristics of the solar cells were measured using a solar simulator ($100 \text{ mW}\cdot\text{cm}^{-2}$, Oriel 94023A, Newport) equipped with a Keithley 2400 digital source meter. The exact light intensity was calibrated using a single-crystal silicon reference photovoltaic cell (91150V, Oriel Instruments).

3. Results and discussion

3.1 Perovskite material tends to accumulate in the upper area of the scaffold film

The $\text{TiO}_2/\text{ZrO}_2$ scaffold film was prepared using the screen-printing technique, and the XRD patterns of both films deposited on the FTO substrate are shown separately in Figure S1. The cross-sectional views of typical scaffold films at high and low magnifications are shown in Figure S2. As can be seen, it exhibits a bilayer morphology, where the bottom TiO_2 layer is fully covered by the upper ZrO_2 layer. In common planar-structure PSCs, a perovskite film thickness of approximately 400 nm is required for sufficient light absorption³⁷. When a comparable amount of perovskite material is incorporated into the scaffold film, its thickness must be significantly increased to the micrometer level. The increased thickness of the scaffold film ensures efficient electron extraction from the perovskite absorber, ultimately reducing hole accumulation and mitigating severe carrier recombination.

Considering that the carbon film has a thickness of tens of micrometers and a pore size in the micrometer range, it barely affects the complete filling of the perovskite material³⁸. Therefore, in the following analysis, the filling behavior is investigated exclusively based on the $\text{TiO}_2/\text{ZrO}_2$ scaffold film. After MAPbI_3 is incorporated into the $\text{TiO}_2/\text{ZrO}_2$ scaffold film, the filling results are characterized by EDS. Seven targets were selected, as shown in Fig. 1(a), with detailed measurement results presented in Table S1. The comparative weight percentage distributions of Ti, Zr, O, Pb, I, Sn, and F from top to bottom in the scaffold film are shown in Fig. 1(b). It is observed that the distribution profiles of Ti and Zr are in good agreement with the morphology results in Fig. 1(a), confirming the validity of the characterization. The distributions of Pb and I were analyzed and found to be mainly concentrated on the upper surface, indicating that MAPbI_3 does not penetrate into the inner part of the scaffold film. A comparative study on a thinner scaffold film was also conducted, as shown in Figure S3. The thickness of the $\text{TiO}_2/\text{ZrO}_2$ scaffold film was reduced from $\sim 8\ \mu\text{m}$ to $\sim 4\ \mu\text{m}$, which is comparable to reported results, yet the perovskite material still cannot penetrate deep into its interior. This suggests that the thickness of the $\text{TiO}_2/\text{ZrO}_2$ scaffold film is not the primary factor determining the filling amount.

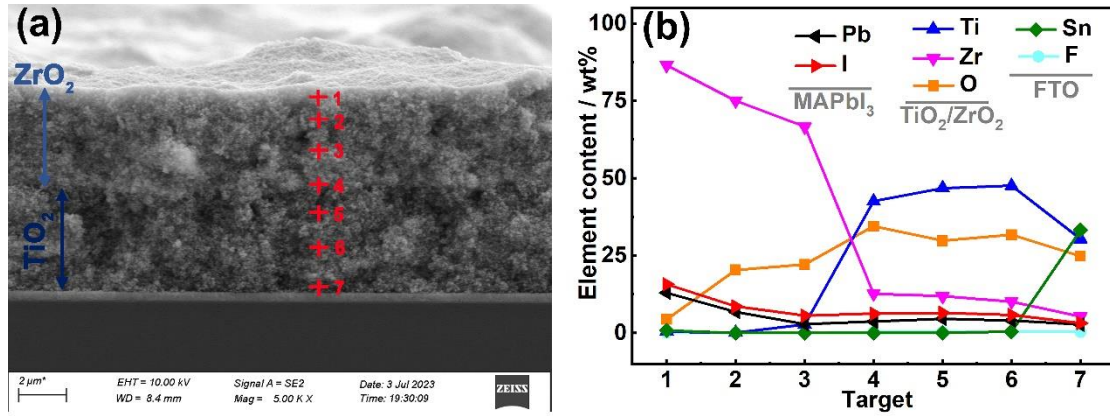


Fig. 1 Cross-sectional view of the TiO₂/ZrO₂ scaffold film filled with MAPbI₃ material, with seven selected targets marked by red crosses for element distribution analysis (a). Comparative weight percentage distribution of representative elements from MAPbI₃, TiO₂/ZrO₂, and FTO, based on targets 1 to 7 (b).

3.2 Optimization of perovskite precursor infiltration is the primary consideration to improve the filling amount

To understand the physical dynamics of the filling process, the infiltration process was first analyzed. The geometric structure of the TiO₂/ZrO₂ scaffold film was constructed for both 3D and 2D TiO₂/ZrO₂ models, as shown in Fig. 2(a) and 2(b). In the model, the lower layer consists of TiO₂, while the upper layer consists of ZrO₂. Since the thickness of the scaffold film ($\sim 7 \mu\text{m}$) is much smaller than the length of the upper surface ($\sim 10 \text{ mm}$), evaporation from the lateral surface of the precursor solution can be neglected. Ideally, the MAPbI₃ solution permeates downward from the surface to the bottom, as illustrated in Fig. 2(c).

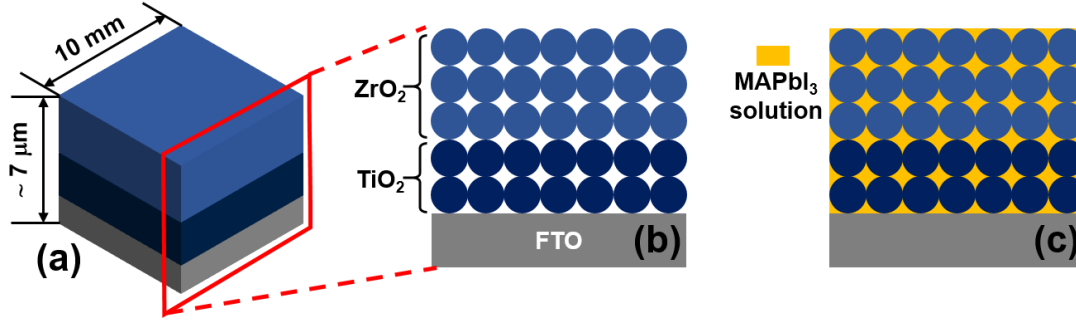


Fig. 2 Geometric structure of the $\text{TiO}_2/\text{ZrO}_2$ scaffold film: (a) 3D model, (b) 2D model, and (c) complete infiltration of the MAPbI_3 precursor solution.

After depositing the MAPbI_3 precursor solution onto the $\text{TiO}_2/\text{ZrO}_2$ scaffold film, the infiltration length of the solution depends on both capillary attraction and evaporation. The evaporation rate of the MAPbI_3 precursor solution, denoted as V_1 , represents the rate at which the DMF solvent evaporates from the solution. Meanwhile, the infiltration rate, denoted as V_2 , represents the rate at which the perovskite precursor solution penetrates the scaffold film due to capillary attraction. These two opposing factors determine the filling amount and can be used to estimate the infiltration state. As shown in Fig. 3: When $V_1 > V_2$, strong evaporation prevents the perovskite precursor solution from penetrating deep into the $\text{TiO}_2/\text{ZrO}_2$ scaffold film, causing the perovskite material to accumulate in the upper region (Fig. 3(a)). When $V_1 = V_2$, the perovskite **precures** or solution crystallizes as it infiltrates, making it difficult for the perovskite material to reach the bottom of the scaffold film (Fig. 3(b)). When $V_1 < V_2$, the perovskite precursor solution has sufficient time to reach the bottom region of the $\text{TiO}_2/\text{ZrO}_2$ scaffold film, leading to deeper infiltration (Fig. 3(c)). If the entire mesoporous $\text{TiO}_2/\text{ZrO}_2$ scaffold film is fully immersed in the MAPbI_3 precursor solution, complete filling may be achieved depending on subsequent crystallization

conditions. Since V_1 is influenced by factors such as the porosity of the mesoporous framework, the wettability of materials, and solvent viscosity, optimizing the infiltration process requires strategies such as increasing pore size, enhancing wettability, and adjusting solvent properties. Additionally, reducing the evaporation rate can further improve infiltration, which can be achieved by conducting experiments in a cold and confined environment. In the following study, two specific strategies are chosen: increasing the pore size and maintaining the ambient temperature at 2–3°C.

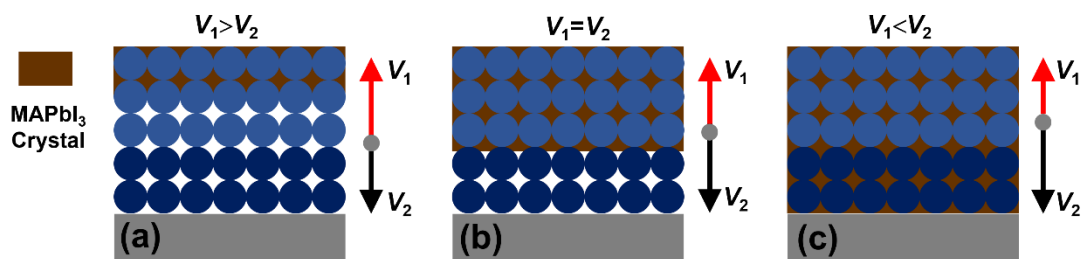


Fig. 3 Infiltration process influenced by the combined effect of both capillarity attraction and evaporation: (a) $V_1 > V_2$, (b) $V_1 = V_2$ and (c) $V_1 < V_2$, where the evaporation rate of DMF solvent is coded as V_1 , and the infiltration rate of the MAPbI₃ precursor solution resulting from capillarity attraction is coded as V_2

3.3 Optimization of perovskite precursor crystallization is the secondary consideration to improve the filling amount

To further understand the physical dynamics of the filling process, the crystallization process was analyzed. The evaporation of the DMF solvent leads to solute accumulation in the upper region, creating a concentration gradient between the upper and bottom areas. As a result, the MAPbI₃ precursor diffuses from the upper region toward the bottom. Additionally, since DMF evaporation is an endothermic process, the temperature in the upper area decreases, forming a temperature gradient

between the upper and bottom regions. Given that the solubility of MAPbI₃ in DMF decreases with decreasing temperature³⁹, the upper area of the precursor solution becomes a preferential site for nucleation. Another preferential nucleation site is the bottom region, as the energy barrier for heterogeneous nucleation is lower than that for homogeneous nucleation⁴⁰.

If the preferential nucleation sites are confined to the upper region, nucleation and growth of the MAPbI₃ precursor will occur sequentially on the surface of the TiO₂/ZrO₂ scaffold film as the DMF solvent evaporates, leading to a top-down crystallization process, as shown in Fig. 4(a). If the crystallization is isotropic, the MAPbI₃ material may cover the entire surface of the TiO₂/ZrO₂ scaffold film. Conversely, if the preferential nucleation sites are located at the bottom, nucleation and growth of the MAPbI₃ precursor will be concentrated in the lower region of the scaffold film. The continuous evaporation of the DMF solvent will provide a driving force for bottom-up crystallization, as shown in Fig. 4(b). In this case, perovskite will precipitate at the bottom of the TiO₂/ZrO₂ scaffold film, and in combination with the bottom-up crystallization process, this can result in complete filling. In the absence of crystallization control, nucleation sites will be randomly distributed, leading to an uncontrolled crystallization process where MAPbI₃ crystals form irregularly throughout the TiO₂/ZrO₂ scaffold film, as illustrated in Fig. 4(c). In the following study, the bottom-up crystallization process, assisted by a low-pressure gas pumping method, is selected.

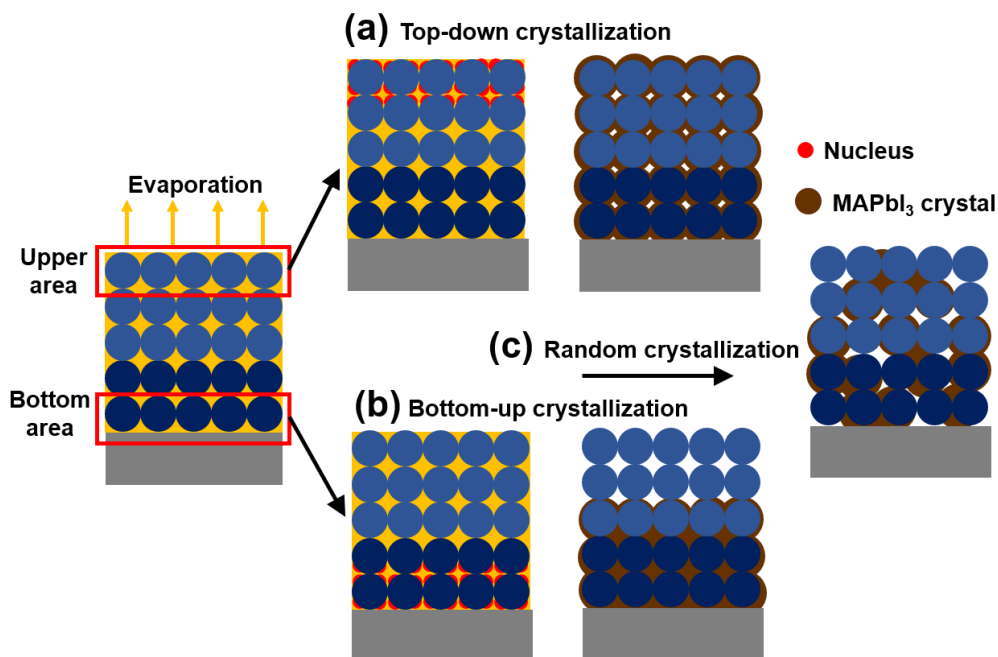


Fig. 4 Preferential nucleation sites and the corresponding filling states of MAPbI₃ based on different crystallization processes: (a) top-down crystallization dependent on the preferential nucleation site in the upper area, (b) bottom-up crystallization dependent on the preferential nucleation site in the bottom area, and (c) random crystallization dependent on uncontrollable nucleation sites.

3.4 The performance of PSCs with enhanced filling and those without enhancement was compared

Monodisperse PS microspheres are a type of material characterized by a highly uniform particle size distribution. They volatilize at temperatures above 200°C. When incorporated into a solid film and subsequently removed through annealing, they allow for direct regulation of the film's pore structure. To optimize the pore structure for enhancing the infiltration of the perovskite precursor solution, PS microspheres with a diameter of 300 nm were selected. The optimal **number** of PS microspheres was determined through modeling calculations to maintain films with suitable porosity. The

detailed modeling and calculation process is provided in the supporting information.

When PS microspheres occupy increases to 30%, based on the experiment, it is found that it results in problems such as powder detachment and delamination of the scaffold film because of the insufficient bonding between particles within the printed scaffold film. Based on these experimental observations, we chose a content of 25% to ensure structural stability.

The cross-sectional view of $\text{TiO}_2/\text{ZrO}_2$ scaffold with 25% porosity is shown in Figure S7.

After the perovskite precursor solution has infiltrated the $\text{TiO}_2/\text{ZrO}_2$ scaffold film with submicron pores, the sample is transferred to a low-pressure chamber to ensure bottom-up crystallization. The element distribution of the final film is monitored using EDS. Eight targets are selected, ranging from the upper area to the bottom area of the film. As shown, the content of Pb and I elements remains nearly constant at 18 wt% and 25 wt%, respectively, from target 1 to target 8. The filling of MAPbI_3 is clearly enhanced from the upper surface to the bottom area of the scaffold layer. This result highlights the importance of dividing the filling process of perovskite materials into two critical stages: the infiltration of the perovskite precursor and the crystallization of the solid perovskite. Complete filling in the first stage, followed by bottom-up crystallization in the second stage, effectively promotes the full filling of perovskite materials.

Rev.2
Com.7

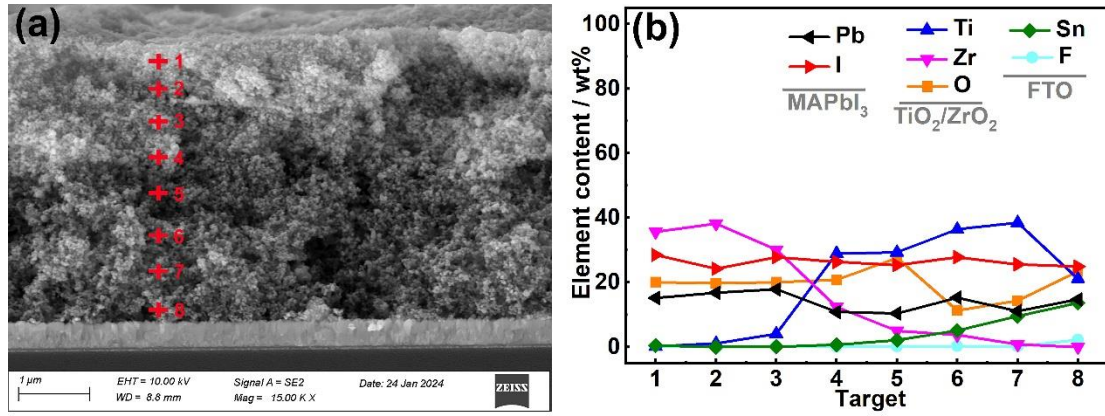


Fig. 5 Cross-sectional view of the TiO₂/ZrO₂ scaffold film with enhanced filling of MAPbI₃ material, showing the eight selected targets marked with red crosses for element distribution tracing (a). Comparative weight percent distribution of representative elements from MAPbI₃, TiO₂/ZrO₂, and FTO based on the targets from 1 to 8 (b).

When both the unenhanced-filling (Un-En) and enhanced-filling (En) scaffold films were assembled into PSCs, the typical photovoltaic performance is shown in Fig. 6. Both PSCs exhibit an open-circuit voltage (V_{oc}) of nearly 1.0 V, indicating that the P-N junction structure is intact and the voltage difference between the photoanode and counter electrode is consistent. However, the En PSC shows a short-circuit current density (J_{sc}) of 19.42 mA·cm⁻² and a fill factor (FF) of 57.51%, whereas the Un-En PSC shows a J_{sc} of 15.84 mA·cm⁻² and an FF of 16.47%. This improvement can be attributed to the enhanced perovskite filling in the scaffold layer, which both increases the light-harvesting capability of the cell and improves the perovskite/TiO₂ interface, facilitating carrier separation and transport while reducing the parallel resistance of the cell. Finally, the En PSC shows a conversion efficiency (η) of 10.60%, which represents a 375% improvement compared to the Un-En PSC. Furthermore, the batch stability of

the cell's photovoltaic performance was tested, as shown in Fig. 7. It can be observed that the mean values are $V_{oc} = 0.98$ V, $J_{sc} = 16.02$ mA·cm⁻², FF = 54.28%, and $\eta = 8.73\%$, demonstrating that enhancing the perovskite filling improves the stability of the cell structure, thereby achieving more stable performance. As a comparison, the same number of Un-En PSCs were also assembled, among which only 9 exhibited measurable conversion efficiency. The performance data of these efficient devices are presented in Figure S9. The poor filling state in the Un-En PSCs fails to provide stable pathways for charge transport, resulting in only a portion of the cells exhibiting low efficiency. The stability performance of the three parallel En PSCs are shown in Figure S8. It can be seen that the unencapsulated cells exhibit minimal performance degradation after being exposed to the ambient environment for 15 days.

Rev.2
Com.6

Rev.1
Com.5

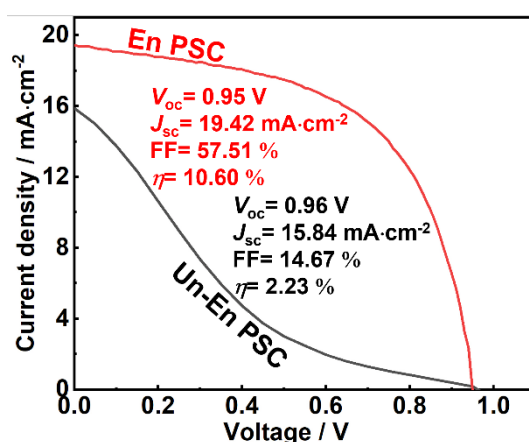


Fig. 6 Typical I - V results of the PSCs with the Un-En film (black line) and En film (red line)

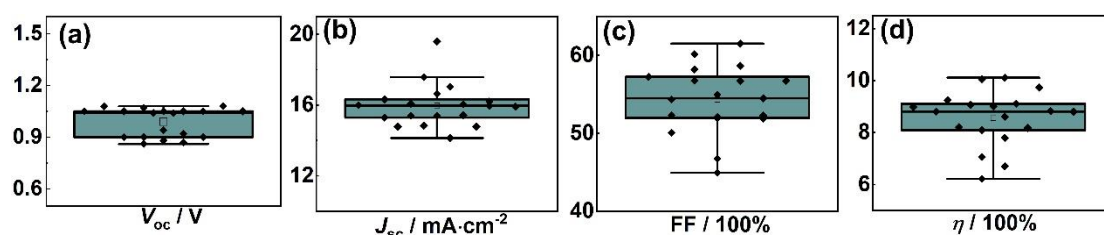


Fig. 7 Statistical results of the photovoltaic performance of the En PSCs: (a) V_{oc} , (b)

J_{sc} , (c) FF and (d) η

4. Conclusion

In this study, the filling results show that MAPbI₃ tends to aggregate in the upper area of the TiO₂/ZrO₂ scaffold film. To enhance the filling of the perovskite material, a physical filling dynamics model has been systematically proposed. This model divides the filling process into two stages: the initial infiltration of the perovskite precursor solution and the subsequent bottom-up crystallization of the perovskite precursor. During the experiment, PS microspheres are introduced to enhance porosity, and the temperature is kept low to restrain the evaporation of the solution. Additionally, bottom-up crystallization control is used to further improve perovskite incorporation into the scaffold layer. The EDS results show that the perovskite material is significantly filled within the inner part of the scaffold layer, and the photovoltaic performance confirms that increasing perovskite filling significantly enhances the conversion efficiency of the cells. In the future, enhancing capillary attraction and reducing evaporation will both contribute to the complete filling of perovskite materials into the active film.

Rev.1
Com.8

Acknowledgements

National Natural Science Foundation of China (Grant No. 62204202), Natural Science Basic Research Program of Shaanxi Province (Grant No. 2024JC-YBMS-438), Youth Innovation Team of Colleges and Universities in Shaanxi Province, The Key Research and Development Program of Shaanxi Program (Grant No. 2023KXJ-172), 2024 Scientific Research Project of Shaanxi Institute of technology (Grant No. Gfy24-04)

Availability of Supporting Data

Several supporting information has been added as a single text.

Conflict of Interest

All the authors declare of no conflict of interest.

Reference

1. Green, M. A.; Dunlop, E. D.; Yoshita, M.; Kopidakis, N.; Bothe, K.; Siefert, G.; Hao, X., Solar cell efficiency tables (version 62). *Prog. Photovolt.: Res. Appl.* **2023**, *31*, 651-663.
2. Chen, B.; Yu, Z.; Onno, A.; Yu, Z.; Chen, S.; Wang, J.; Holman, Z. C.; Huang, J., Bifacial all-perovskite tandem solar cells. *Sci. Adv.* **2022**, *8*, eadd0377.
3. Ku, Z.; Rong, Y.; Xu, M.; Liu, T.; Han, H., Full Printable processed mesoscopic CH₃NH₃PbI₃/TiO₂ heterojunction solar cells with carbon counter electrode. *Sci. Rep.* **2013**, *3*, 3132.
4. Mei, A.; Li, X.; Liu, L.; Ku, Z.; Liu, T.; Rong, Y.; Xu, M.; Hu, M.; Chen, J.; Yang, Y.; Grätzel, M.; Han, H., A hole-conductor-free, fully printable mesoscopic perovskite solar cell with high stability. *Science* **2014**, *345*, 295-298.
5. Liu, L.; Mei, A.; Liu, T.; Jiang, P.; Sheng, Y.; Zhang, L.; Han, H., Fully printable mesoscopic perovskite solar cells with organic silane self-assembled monolayer. *J. Am. Chem. Soc.* **2015**, *137*, 1790-1793.
6. Hu, Y.; Si, S.; Mei, A.; Rong, Y.; Liu, H.; Li, X.; Han, H., Stable large-area (10 × 10 cm²) printable mesoscopic perovskite module exceeding 10% efficiency. *Solar RRL* **2017**, *1*, 1600019.
7. Fu, Z.; Xu, M.; Sheng, Y.; Yan, Z.; Meng, J.; Tong, C.; Li, D.; Wan, Z.; Ming, Y.; Mei, A.; Hu, Y.; Rong, Y.; Han, H., Encapsulation of printable mesoscopic

- perovskite solar cells enables high temperature and long-term outdoor stability. *Adv. Funct. Mater.* **2019**, *29*, 1809129.
8. Mei, A.; Sheng, Y.; Ming, Y.; Hu, Y.; Rong, Y.; Zhang, W.; Luo, S.; Na, G.; Tian, C.; Hou, X.; Xiong, Y.; Zhang, Z.; Liu, S.; Uchida, S.; Kim, T.-W.; Yuan, Y.; Zhang, L.; Zhou, Y.; Han, H., Stabilizing perovskite solar cells to IEC61215:2016 standards with over 9,000-h operational tracking. *Joule* **2020**, *4*, 2646-2660.
 9. Rong, Y.; Hu, Y.; Mei, A.; Tan, H.; Saidaminov, M. I.; Seok, S. I.; McGehee, M. D.; Sargent, E. H.; Han, H., Challenges for commercializing perovskite solar cells. *Science* **2018**, *361*, 5978.
 10. Ito, S.; Tsuji, R. Mesoscopic anodes and cathodes for printable perovskite solar cells. 2023, Chapter 4.
 11. Yao, Z.; Ning, Z. A breakthrough of printable mesoscopic perovskite solar cells. *Sci. Chi. Mater.* **2025**, *68*, 307-308.
 12. Cao, K.; Zuo, Z.; Cui, J.; Shen, Y.; Moehl, T.; Zakeeruddin, S. M.; Grätzel, M.; Wang, M., Efficient screen printed perovskite solar cells based on mesoscopic TiO₂/Al₂O₃/NiO/carbon architecture. *Nano Energ.* **2015**, *17*, 171-179.
 13. Duan, M.; Rong, Y.; Mei, A.; Hu, Y.; Sheng, Y.; Guan, Y.; Han, H., Efficient hole-conductor-free, fully printable mesoscopic perovskite solar cells with carbon electrode based on ultrathin graphite. *Carbon* **2017**, *120*, 71-76.
 14. Jiang, P.; Jones, T. W.; Duffy, N. W.; Anderson, K. F.; Bennett, R.; Grigore, M.; Marvig, P.; Xiong, Y.; Liu, T.; Sheng, Y.; Hong, L.; Hou, X.; Duan, M.; Hu, Y.; Rong, Y.; Wilson, G. J.; Han, H., Fully printable perovskite solar cells with highly-

- conductive, low-temperature, perovskite-compatible carbon electrode. *Carbon* **2018**, *129*, 830-836.
15. Xu, C.; Zhang, Z.; Hu, Y.; Sheng, Y.; Jiang, P.; Han, H.; Zhang, J., Printed hole-conductor-free mesoscopic perovskite solar cells with excellent long-term stability using PEAI as an additive. *J. Energ. Chem.* **2018**, *27*, 764-768.
 16. Jeon, N. J.; Noh, J. H.; Kim, Y. C.; Yang, W. S.; Ryu, S.; Seok, S. I., Solvent engineering for high-performance inorganic–organic hybrid perovskite solar cells. *Nat. Mater.* **2014**, *13*, 897-903.
 17. Wu, Y.; Islam, A.; Yang, X.; Qin, C.; Liu, J.; Zhang, K.; Peng, W.; Han, L., Retarding the crystallization of PbI₂ for highly reproducible planar-structured perovskite solar cells via sequential deposition. *Energ. Environ. Sci.* **2014**, *7*, 2934-2938.
 18. Ahn, N.; Son, D.-Y.; Jang, I.-H.; Kang, S. M.; Choi, M.; Park, N.-G., Highly reproducible perovskite solar cells with average efficiency of 18.3% and best efficiency of 19.7% fabricated via lewis base adduct of lead(II) iodide. *J. Am. Chem. Soc.* **2015**, *137*, 8696-8699.
 19. Hou, X.; Xu, M.; Tong, C.; Ji, W.; Fu, Z.; Wan, Z.; Hao, F.; Ming, Y.; Liu, S.; Hu, Y.; Han, H.; Rong, Y.; Yao, Y., High performance printable perovskite solar cells based on Cs_{0.1}FA_{0.9}PbI₃ in mesoporous scaffolds. *J. Power Sources* **2019**, *415*, 105-111.
 20. Chen, J.; Rong, Y.; Mei, A.; Xiong, Y.; Liu, T.; Sheng, Y.; Jiang, P.; Hong, L.; Guan, Y.; Zhu, X.; Hou, X.; Duan, M.; Zhao, J.; Li, X.; Han, H., Hole-conductor-free

- dually printable mesoscopic solar cell with mixed-anion perovskite $\text{CH}_3\text{NH}_3\text{PbI}_{(3-x)}(\text{BF}_4)_x$. *Adv. Energ. Mater.* **2016**, *6*, 1502009.
21. Wang, Q.; Zhang, W.; Zhang, Z.; Liu, S.; Wu, J.; Guan, Y.; Mei, A.; Rong, Y.; Hu, Y.; Han, H., Crystallization control of ternary-cation perovskite absorber in triple-mesoscopic layer for efficient solar cells. *Adv. Energ. Mater.* **2020**, *10*, 1903092.
 22. Saliba, M.; Matsui, T.; Seo, J.-Y.; Domanski, K.; Correa-Baena, J.-P.; Nazeeruddin, M. K.; Zakeeruddin, S. M.; Tress, W.; Abate, A.; Hagfeldt, A.; Grätzel, M., Cesium-containing triple cation perovskite solar cells: improved stability, reproducibility and high efficiency. *Energ. Environ. Sci.* **2016**, *9*, 1989-1997.
 23. Saliba, M.; Matsui, T.; Domanski, K.; Seo, J.-Y.; Ummadisingu, A.; Zakeeruddin, S. M.; Correa-Baena, J.-P.; Tress, W. R.; Abate, A.; Hagfeldt, A.; Grätzel, M., Incorporation of rubidium cations into perovskite solar cells improves photovoltaic performance. *Science* **2016**, *354*, 206-209.
 24. Xiang, J.; Han, C.; Cheng, Y.; Gao, Q.; Hu, W.; Zhou, Y.; Mei, A.; Zhou, Y.; Han, H. Recent progress and advances of perovskite crystallization in carbon-based printable mesoscopic solar cells. *Adv. Mater.* **2025**, 2415405.
 25. Li, F.; Lin, F. R.; Jen, A. K. Y. Current state and future perspectives of printable organic and perovskite solar cells. *Adv. Mater.* **2024**, *36*, 2307161.
 26. Yang, H.; Zhao, J.; Zhou, T.; Zhang, H.; Zhang, W.; Zhang, J.; Hu, G.; Zhang, Y.; Liu, Q. Mesoporous TiO_2 electron transport materials derived from 2D Ti-MOFs for enhanced power conversion efficiency in Pprinted mesoscopic perovskite solar cells. *ACS Appl. Nano Mater.* **2023**, *6*, 16353-16361.

27. Worsley, C. A.; Dunlop, T. O.; Potts, S.-J.; Garcia-Rodriguez, R.; Bolton, R. S.; Davies, M. L.; Jewell, E.; Watson, T. M. Quantifying infiltration for quality control in printed mesoscopic perovskite solar cells: a microscopic perspective. *ACS Appl. Energ. Mater.* **2024**, *7*, 1938-1948.
28. Xiang, J.; Han, C.; Qi, J.; Cheng, Y.; Chen, K.; Ma, Y.; Xie, J.; Hu, Y.; Mei, A.; Zhou, Y. A Polymer defect passivator for efficient hole-conductor-free printable mesoscopic perovskite solar cells. *Adv. Funct. Mater.* **2023**, *33*, 2300473.
29. Wang, H.; Yang, F.; Li, X.; Zhang, P. Fully printed high-performance quasi-two-dimensional perovskite solar cells via multifunctional interfacial engineering. *Adv. Funct. Mater.* **2024**, *34*, 2312250.
30. Chen, J.; Xiong, Y.; Rong, Y.; Mei, A.; Sheng, Y.; Jiang, P.; Hu, Y.; Li, X.; Han, H., Solvent effect on the hole-conductor-free fully printable perovskite solar cells. *Nano Energ.* **2016**, *27*, 130-137.
31. Rong, Y.; Venkatesan, S.; Guo, R.; Wang, Y.; Bao, J.; Li, W.; Fan, Z.; Yao, Y., Critical kinetic control of non-stoichiometric intermediate phase transformation for efficient perovskite solar cells. *Nanoscale* **2016**, *8*, 12892-12899.
32. Jiang, Z.; Wang, B.; Zhang, W.; Yang, Z.; Li, M.; Ren, F.; Imran, T.; Sun, Z.; Zhang, S.; Zhang, Y.; Zhao, Z.; Liu, Z.; Chen, W., Solvent engineering towards scalable fabrication of high-quality perovskite films for efficient solar modules. *J. Energ. Chem.* **2023**, *80*, 689-710.
33. Bogachuk, D.; Girard, J.; Tilala, S.; Martineau, D.; Narbey, S.; Verma, A.; Hinsch, A.; Kohlstädt, M.; Wagner, L. Nanoarchitectonics in fully printed perovskite solar

- cells with carbon-based electrodes. *Nanoscale* **2023**, *15*, 3130-3134.
34. Gao L.; Yang G. J. Organic-inorganic halide perovskites: from crystallization of polycrystalline films to solar cell applications *Solar RRL* **2019**, *12*, 1900200.
 35. Ding B.; Li Y.; Huang S. Y.; Chu Q. Q.; Li C. X.; Li C. J.; Yang G. J.; Material nucleation/growth competition tuning towards highly reproducible planar perovskite solar cells with efficiency exceeding 20% *J. Mater. Chem. A* **2017**, *5*, 6840-6848.
 36. Ding B.; Gao L. L.; Liang L. S.; Chu Q. Q.; Song X. X.; Li Y.; Yang G. J.; Fan B.; Wang M. K.; Li C. X.; Li C. J. Facile and scalable fabrication of highly efficient lead iodide perovskite thin-film solar cells in air using gas pump method, *ACS Appl. Mater. Interf.* **2016**, *8*, 20067-20073.
 37. Zhao, Y.; Zhu, K., Solution chemistry engineering toward high-efficiency perovskite solar cells. *J. Phys. Chem. Lett.* **2014**, *5*, 4175-4186.
 38. Han, H.; Bach, U.; Cheng, Y.-B.; Caruso, R. A.; MacRae, C., A design for monolithic all-solid-state dye-sensitized solar cells with a platinized carbon counterelectrode. *Appl. Phys. Lett.* **2009**, *94*, 103102.
 39. Heo, J. H.; Song, D. H.; Im, S. H., Planar CH₃NH₃PbBr₃ hybrid solar cells with 10.4% power conversion efficiency, fabricated by controlled crystallization in the spin-coating process. *Adv. Mater.* **2014**, *26*, 8179-8183.
 40. Li, Y.; Li, X.; Chu, Q.; Dong, H.; Yao, J.; Zhou, Y.; Yang, G., Tuning nucleation sites to enable monolayer perovskite films for highly efficient perovskite solar cells. *Coatings* **2018**, *8*, 408.

-
- $\text{CH}_3\text{NH}_3\text{PbI}_3$ aggregates at the upper area of $\text{TiO}_2/\text{ZrO}_2$ scaffold film.
 - Filling process should be divided into infiltration and precipitation.
 - Increasing pore size combined with bottom-up crystallization promote filling.
 - η of En PSC improves by 375% compared with Un-En PSC.

Enhancing the filling of perovskite material in the scaffold layer to improve the conversion efficiency of printable perovskite solar cells

Weiwu Dang¹, Li Liu², Jianhua Chen², Xian Gu², Xuhao Wang², Xiaolan Li²,

Yan Li^{2, *}

¹College of Intelligent Manufacturing, Shaanxi Institute of Technology, Xi'an, Shaanxi 710300, China

²College of New Energy, Xi'an Shiyou University, Xi'an, Shaanxi 710065, China

* Correspondence to: Doc. Yan Li, College of New Energy, Xi'an Shiyou University, Xi'an, Shaanxi 710065, China

E-mail address: li1988yan@163.com

Abstract: The complete filling of perovskite materials into mesoporous TiO₂/ZrO₂ scaffold film remains a great challenge for achieving a high conversion efficiency in printed mesoscopic perovskite solar cells. However, there is a lack of a precise understanding of the filling dynamics to guide the optimization process. In this study, a process comprising the beginning infiltration step and the subsequent crystallization step have been proposed to optimize filling behavior. By introducing macropores in the first step using the polystyrene microsphere templating method to facilitate the infiltration of the perovskite precursor solution, combined with the bottom-up controlled crystallization assisted by a low-pressure gas pumping method in the second step, the perovskite material is more completely filled into the TiO₂/ZrO₂ scaffold layer. The photovoltaic performance of the perovskite solar cell shows that the conversion efficiency is improved by 375% compared to the weakly filled solar cells. This work contributes to enhance the filling of perovskite

material and improve the conversion efficiency of printable perovskite solar cells.

Keywords: Printed mesoscopic perovskite solar cells; Filling dynamics; Infiltration; Crystallization

1. Introduction

The commercial-scale production of perovskite solar cells (PSCs) has attracted widespread attention^{1,2}. The printed mesoscopic PSCs with an all-mesoporous structure can be directly fabricated in the air using a screen printing technique³⁻⁵, which is a promising candidate for the commercialization of solar cells. Years ago, when Han's group⁶ introduced $(5\text{-AVA})_x\text{CH}_3\text{NH}_3(1-x)\text{PbI}_3$ as the light-absorbing material, achieving a conversion efficiency of 10.4% in solar cells with an active cell area of 49 cm². Furthermore, it has been reported that the printed mesoscopic PSCs can keep their initial efficiency unchanged during 1000 hours of light exposure, and these solar cells exhibit long-term stability, lasting over one year in the dark due to the hydrophobic nature of carbon electrodes⁶. Studies also indicate that these solar cells retain more than 97% of their initial efficiency after 2,136 hours under outdoor conditions⁷, and the printable PSCs have passed the widely recognized international standard IEC61215:2016⁸. Nowadays, Wonder Solar Ltd. demonstrates a 110 m² fully printable mesoscopic PSCs outdoor power generation system⁹. Researchers believe that printable mesoscopic PSCs are strong contenders for the commercialization of perovskite solar cells.^{10,11}

In the printed mesoscopic PSCs, removing the hole transport material and replacing the silver/gold electrode with a carbon electrode can reduce the cost of the solar cells and simplify the fabrication process¹²⁻¹⁵. However, preparation of the carbon electrode requires a high-temperature treatment at 400°C, which is higher than the decomposition temperature of the perovskite materials. Therefore, in the solar cell assembly process, the carbon electrode is first deposited onto the TiO₂/ZrO₂ scaffold layer, after which the perovskite, serving as the light-absorbing material, is infiltrated into the scaffold film using a solution-based method¹⁶⁻¹⁸. However, the extent to which perovskite fills the scaffold film is crucial for the performance and stability of the fully printable PSCs¹⁹⁻²¹. A completely filling and good connectivity of the perovskite material in the scaffold film enhances its ability to capture photonic energy, dissociating excitons via the MAPbI₃/TiO₂ heterojunction, and transport holes to carbon electrode, whereas insufficient filling of the perovskite material in the TiO₂/ZrO₂ scaffold film leads to poor light absorption, discontinuous carrier transport channels, and severe internal recombination^{22,23}.

The filling amount of perovskite material is influenced by multiple factors, such as the uncontrolled crystallization of the precursor solution²⁴, the pore structure of the mesoporous scaffold layer^{25,26}, the filling process²⁷ and the interfacial contact between the perovskite and the mesoporous scaffold layer^{28,29}. Many researchers have attempted to manipulate the perovskite precursor, such as Chen et al.³⁰ systematically investigated the impact of various solvents on the filling behavior, and achieved a conversion efficiency of 13.89% by optimizing the ratio of N,N-dimethylformamide (C₃H₇NO,

DMF) and dimethyl sulfoxide (C_2H_6OS , DMSO). This optimization improved the wettability and stabilized the mesophase of the perovskite precursor, thereby regulating the crystallization rate of perovskite crystals. Rong et al.³¹ utilized pure DMSO as a solvent due to its strong coordination ability and the formation of a stable intermediate phase (PbI_2 -DMSO- CH_3NH_3I) to dissolve perovskite. This approach effectively inhibited the rapid binding of PbI_2 and CH_3NH_3I while accelerating the infiltration of the perovskite precursor into the scaffold layer. In addition to the manipulation of the solvent, previous results have demonstrated that both pore blockage caused by preferential perovskite crystallization and solvent retention can lead to incomplete filling of the scaffold film³². Bogachuk et al.³³ introduced a sacrificial Polystyrene nanoparticles film into the scaffold film to create nano-cavities enabling the growth of larger perovskite crystals inside the oxide scaffold. However, achieving complete filling of perovskite materials into the TiO_2/ZrO_2 scaffold film is still a great challenge. To reach a fully filled state, a precise understanding of the physical dynamics involved is still required. Moreover, the correlation between solution infiltration and precursor crystallization has yet to be fully established, and the corresponding regulatory mechanisms governing these processes remain unexplored.

In the study, based on the observed filling behavior of $CH_3NH_3PbI_3$ ($MAPbI_3$) into the TiO_2/ZrO_2 scaffold film, the physical filling dynamics were analyzed. The correlation between infiltration and crystallization in enhancing the perovskite materials filling was established. To optimize this process, sub-macropores were introduced into the scaffold layer using the Polystyrene microsphere templating method,

and followed by bottom-up controlled crystallization facilitated by a low-pressure gas pumping method. At last, the photovoltaic performance of the PSCs was evaluated.

2. Experimental

2.1 Materials

Zirconium oxide (ZrO_2) powder and titanium dioxide (TiO_2) powder were purchased from Degussa AG (Germany). N-butanol ($\text{C}_4\text{H}_{10}\text{O}$), terpineol ($\text{C}_{10}\text{H}_{18}\text{O}$), ethyl cellulose ($((\text{C}_{12}\text{H}_{22}\text{O}_5)_n)$) and acetone ($\text{C}_3\text{H}_6\text{O}$) were purchased from Shanghai Reagent Chemical Co., Ltd (China). Lead iodide (PbI_2), methylamine iodide ($\text{CH}_3\text{NH}_3\text{I}$, MAI), DMF, TiO_2 compact layer precursor solution and Carbon electrode material were purchased from Xi'an Yuri Solar Co., Ltd (China). The transparent fluorine-doped tin oxide (FTO, TEC-15, $25 \times 25 \text{ mm}^2$, LOF) conductive glass was used as substrates. The polystyrene (PS) microspheres of $\sim 300 \text{ nm}$ were purchased from Rigor Science Co., Ltd (China).

2.2 Preparation of the TiO_2 and ZrO_2 slurry

For the ZrO_2 slurry, firstly, 0.45 g of ethyl cellulose and 0.6 ml terpineol was dissolved into 5 ml of n-butanol to prepare an ethyl cellulose solution, and 2.5 g of ZrO_2 was dispersed in n-butanol to form a 35 wt% suspension. Secondly, the ethyl cellulose solution and ZrO_2 suspension were mixed by magnetic stirring for 12 h, followed by grinding for 20 min to obtain a ZrO_2 slurry. In order to increase the porosity of the ZrO_2 film by 25%, 0.16 g of PS microspheres was added in the second step.

For the TiO_2 slurry, except that 1.5 g of TiO_2 was dispersed in n-butanol to form a 20 wt% suspension in the first step, the other steps follow the same preparation process

as ZrO₂ slurry. In order to increase the porosity of the TiO₂ film by 25%, 0.07 g of PS microspheres was added in the second step.

2.3 Filling the perovskite into the scaffold film and fabrication of the PSCs

The FTO was cleaned successively in deionized water and alcohol, and dried with N₂ flow. A compact TiO₂ layer was deposited on the etched FTO substrate via spin coating and then annealed at 120°C for 15 min. Subsequently, the TiO₂ films and ZrO₂ films were deposited using screen-printing technique, and then annealed in a tube furnace at 400°C for 30 min to produce the TiO₂/ZrO₂ scaffold films. Then, the carbon film was also deposited using screen-printing technique, and annealed in a tube furnace at 450°C for 30 min.

The MAPbI₃ precursor solution was prepared by dissolving PbI₂ and CH₃NH₃I in DMF at a concentration of 460 mg·mL⁻¹, which was infiltrated from the carbon side, and subsequently spin-coated at 3000 rpm for 10 s. To keep the bottom-up crystallization of the perovskite material, the sample was transferred to the low-pressure chamber of the low-pressure gas pumping equipment³⁴⁻³⁶ and dried at 1000 Pa for 10 min. All the above processes were carried out at a low temperature of 2-3°C. Finally, the PSCs were annealed at 120°C for 10 min. For current density-voltage (*J-V*) characteristics, the cell has an area of 1 × 1 cm², with a TiO₂/ZrO₂ scaffold layer thickness of 4 ± 0.5 μm and a carbon electrode thickness of 15 ± 1 μm.

2.4 Characterization

The phase structures of the TiO₂ and ZrO₂ films were measured by an X-ray diffractometer using Cu K_α radiation (XRD, Bruker-D8 ADVANCE, Germany). The

morphology of the scaffold film was characterized using a scanning electron microscope (SEM, ZEISS Sigma 300, Germany). To quantitatively analyze the elemental distribution in perovskite, energy-dispersive X-ray spectroscopy (EDS, Oxford Xplore 30, United Kingdom) was employed. The J - V characteristics of the solar cells were measured using a solar simulator ($100 \text{ mW}\cdot\text{cm}^{-2}$, Oriel 94023A, Newport) equipped with a Keithley 2400 digital source meter. The exact light intensity was calibrated using a single-crystal silicon reference photovoltaic cell (91150V, Oriel Instruments).

3. Results and discussion

3.1 Perovskite material tends to accumulate in the upper area of the scaffold film

The $\text{TiO}_2/\text{ZrO}_2$ scaffold film was prepared using the screen-printing technique, and the XRD patterns of both films deposited on the FTO substrate are shown separately in Figure S1. The cross-sectional views of typical scaffold films at high and low magnifications are shown in Figure S2. As can be seen, it exhibits a bilayer morphology, where the bottom TiO_2 layer is fully covered by the upper ZrO_2 layer. In common planar-structure PSCs, a perovskite film thickness of approximately 400 nm is required for sufficient light absorption³⁷. When a comparable amount of perovskite material is incorporated into the scaffold film, its thickness must be significantly increased to the micrometer level. The increased thickness of the scaffold film ensures efficient electron extraction from the perovskite absorber, ultimately reducing hole accumulation and mitigating severe carrier recombination.

Considering that the carbon film has a thickness of tens of micrometers and a pore size in the micrometer range, it barely affects the complete filling of the perovskite material³⁸. Therefore, in the following analysis, the filling behavior is investigated exclusively based on the $\text{TiO}_2/\text{ZrO}_2$ scaffold film. After MAPbI_3 is incorporated into the $\text{TiO}_2/\text{ZrO}_2$ scaffold film, the filling results are characterized by EDS. Seven targets were selected, as shown in Fig. 1(a), with detailed measurement results presented in Table S1. The comparative weight percentage distributions of Ti, Zr, O, Pb, I, Sn, and F from top to bottom in the scaffold film are shown in Fig. 1(b). It is observed that the distribution profiles of Ti and Zr are in good agreement with the morphology results in Fig. 1(a), confirming the validity of the characterization. The distributions of Pb and I were analyzed and found to be mainly concentrated on the upper surface, indicating that MAPbI_3 does not penetrate into the inner part of the scaffold film. A comparative study on a thinner scaffold film was also conducted, as shown in Figure S3. The thickness of the $\text{TiO}_2/\text{ZrO}_2$ scaffold film was reduced from $\sim 8\ \mu\text{m}$ to $\sim 4\ \mu\text{m}$, which is comparable to reported results, yet the perovskite material still cannot penetrate deep into its interior. This suggests that the thickness of the $\text{TiO}_2/\text{ZrO}_2$ scaffold film is not the primary factor determining the filling amount.

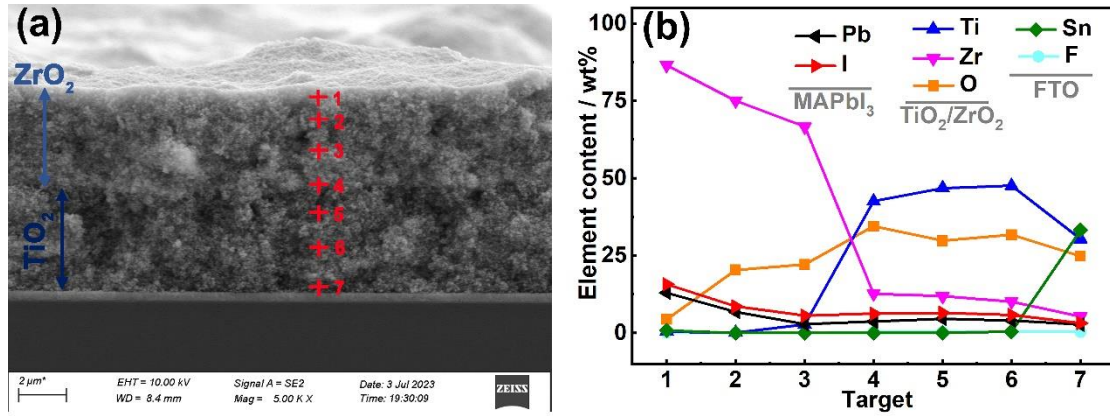


Fig. 1 Cross-sectional view of the TiO₂/ZrO₂ scaffold film filled with MAPbI₃ material, with seven selected targets marked by red crosses for element distribution analysis (a). Comparative weight percentage distribution of representative elements from MAPbI₃, TiO₂/ZrO₂, and FTO, based on targets 1 to 7 (b).

3.2 Optimization of perovskite precursor infiltration is the primary consideration to improve the filling amount

To understand the physical dynamics of the filling process, the infiltration process was first analyzed. The geometric structure of the TiO₂/ZrO₂ scaffold film was constructed for both 3D and 2D TiO₂/ZrO₂ models, as shown in Fig. 2(a) and 2(b). In the model, the lower layer consists of TiO₂, while the upper layer consists of ZrO₂. Since the thickness of the scaffold film (~7 μm) is much smaller than the length of the upper surface (~10 mm), evaporation from the lateral surface of the precursor solution can be neglected. Ideally, the MAPbI₃ solution permeates downward from the surface to the bottom, as illustrated in Fig. 2(c).

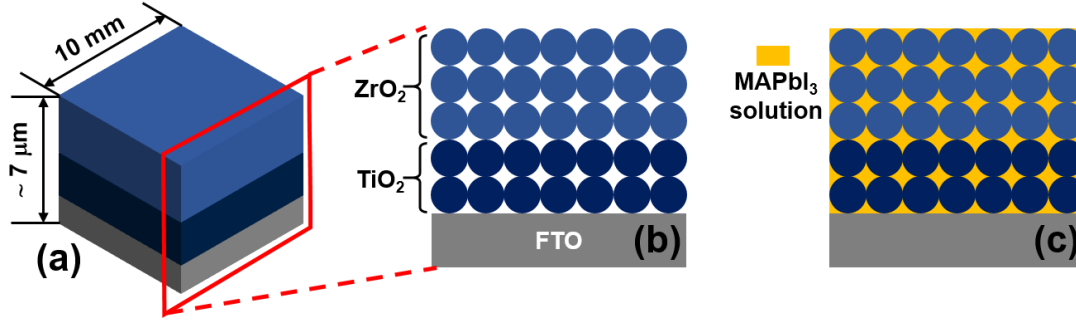


Fig. 2 Geometric structure of the $\text{TiO}_2/\text{ZrO}_2$ scaffold film: (a) 3D model, (b) 2D model, and (c) complete infiltration of the MAPbI_3 precursor solution.

After depositing the MAPbI_3 precursor solution onto the $\text{TiO}_2/\text{ZrO}_2$ scaffold film, the infiltration length of the solution depends on both capillary attraction and evaporation. The evaporation rate of the MAPbI_3 precursor solution, denoted as V_1 , represents the rate at which the DMF solvent evaporates from the solution. Meanwhile, the infiltration rate, denoted as V_2 , represents the rate at which the perovskite precursor solution penetrates the scaffold film due to capillary attraction. These two opposing factors determine the filling amount and can be used to estimate the infiltration state. As shown in Fig. 3: When $V_1 > V_2$, strong evaporation prevents the perovskite precursor solution from penetrating deep into the $\text{TiO}_2/\text{ZrO}_2$ scaffold film, causing the perovskite material to accumulate in the upper region (Fig. 3(a)). When $V_1 = V_2$, the perovskite precursor solution crystallizes as it infiltrates, making it difficult for the perovskite material to reach the bottom of the scaffold film (Fig. 3(b)). When $V_1 < V_2$, the perovskite precursor solution has sufficient time to reach the bottom region of the $\text{TiO}_2/\text{ZrO}_2$ scaffold film, leading to deeper infiltration (Fig. 3(c)). If the entire mesoporous $\text{TiO}_2/\text{ZrO}_2$ scaffold film is fully immersed in the MAPbI_3 precursor solution, complete filling may be achieved depending on subsequent crystallization

conditions. Since V_1 is influenced by factors such as the porosity of the mesoporous framework, the wettability of materials, and solvent viscosity, optimizing the infiltration process requires strategies such as increasing pore size, enhancing wettability, and adjusting solvent properties. Additionally, reducing the evaporation rate can further improve infiltration, which can be achieved by conducting experiments in a cold and confined environment. In the following study, two specific strategies are chosen: increasing the pore size and maintaining the ambient temperature at 2–3°C.

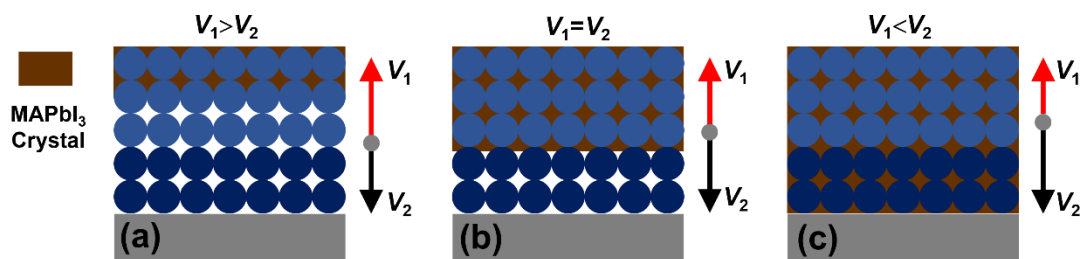


Fig. 3 Infiltration process influenced by the combined effect of both capillarity attraction and evaporation: (a) $V_1 > V_2$, (b) $V_1 = V_2$ and (c) $V_1 < V_2$, where the evaporation rate of DMF solvent is coded as V_1 , and the infiltration rate of the MAPbI₃ precursor solution resulting from capillarity attraction is coded as V_2

3.3 Optimization of perovskite precursor crystallization is the secondary consideration to improve the filling amount

To further understand the physical dynamics of the filling process, the crystallization process was analyzed. The evaporation of the DMF solvent leads to solute accumulation in the upper region, creating a concentration gradient between the upper and bottom areas. As a result, the MAPbI₃ precursor diffuses from the upper region toward the bottom. Additionally, since DMF evaporation is an endothermic process, the temperature in the upper area decreases, forming a temperature gradient

between the upper and bottom regions. Given that the solubility of MAPbI₃ in DMF decreases with decreasing temperature³⁹, the upper area of the precursor solution becomes a preferential site for nucleation. Another preferential nucleation site is the bottom region, as the energy barrier for heterogeneous nucleation is lower than that for homogeneous nucleation⁴⁰.

If the preferential nucleation sites are confined to the upper region, nucleation and growth of the MAPbI₃ precursor will occur sequentially on the surface of the TiO₂/ZrO₂ scaffold film as the DMF solvent evaporates, leading to a top-down crystallization process, as shown in Fig. 4(a). If the crystallization is isotropic, the MAPbI₃ material may cover the entire surface of the TiO₂/ZrO₂ scaffold film. Conversely, if the preferential nucleation sites are located at the bottom, nucleation and growth of the MAPbI₃ precursor will be concentrated in the lower region of the scaffold film. The continuous evaporation of the DMF solvent will provide a driving force for bottom-up crystallization, as shown in Fig. 4(b). In this case, perovskite will precipitate at the bottom of the TiO₂/ZrO₂ scaffold film, and in combination with the bottom-up crystallization process, this can result in complete filling. In the absence of crystallization control, nucleation sites will be randomly distributed, leading to an uncontrolled crystallization process where MAPbI₃ crystals form irregularly throughout the TiO₂/ZrO₂ scaffold film, as illustrated in Fig. 4(c). In the following study, the bottom-up crystallization process, assisted by a low-pressure gas pumping method, is selected.

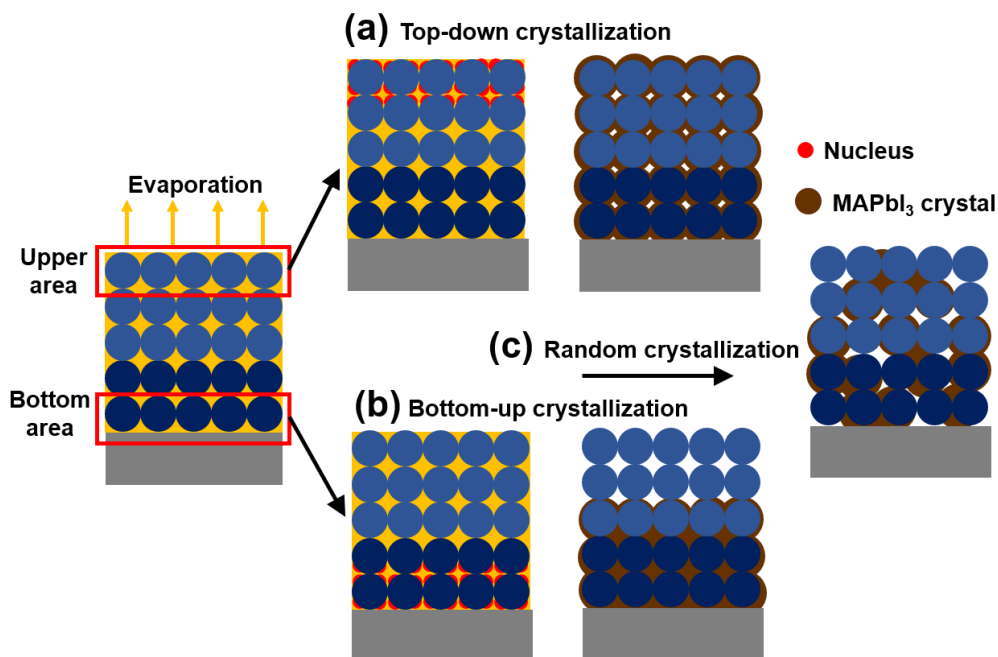


Fig. 4 Preferential nucleation sites and the corresponding filling states of MAPbI₃ based on different crystallization processes: (a) top-down crystallization dependent on the preferential nucleation site in the upper area, (b) bottom-up crystallization dependent on the preferential nucleation site in the bottom area, and (c) random crystallization dependent on uncontrollable nucleation sites.

3.4 The performance of PSCs with enhanced filling and those without enhancement was compared

Monodisperse PS microspheres are a type of material characterized by a highly uniform particle size distribution. They volatilize at temperatures above 200°C. When incorporated into a solid film and subsequently removed through annealing, they allow for direct regulation of the film's pore structure. To optimize the pore structure for enhancing the infiltration of the perovskite precursor solution, PS microspheres with a diameter of 300 nm were selected. The optimal number of PS microspheres was determined through modeling calculations to maintain films with suitable porosity. The

detailed modeling and calculation process is provided in the supporting information. When PS microspheres occupy increases to 30%, based on the experiment, it is found that it results in problems such as powder detachment and delamination of the scaffold film because of the insufficient bonding between particles within the printed scaffold film. Based on these experimental observations, we chose a content of 25% to ensure structural stability. The cross-sectional view of $\text{TiO}_2/\text{ZrO}_2$ scaffold with 25% porosity is shown in Figure S7.

After the perovskite precursor solution has infiltrated the $\text{TiO}_2/\text{ZrO}_2$ scaffold film with submicron pores, the sample is transferred to a low-pressure chamber to ensure bottom-up crystallization. The element distribution of the final film is monitored using EDS. Eight targets are selected, ranging from the upper area to the bottom area of the film. As shown, the content of Pb and I elements remains nearly constant at 18 wt% and 25 wt%, respectively, from target 1 to target 8. The filling of MAPbI_3 is clearly enhanced from the upper surface to the bottom area of the scaffold layer. This result highlights the importance of dividing the filling process of perovskite materials into two critical stages: the infiltration of the perovskite precursor and the crystallization of the solid perovskite. Complete filling in the first stage, followed by bottom-up crystallization in the second stage, effectively promotes the full filling of perovskite materials.

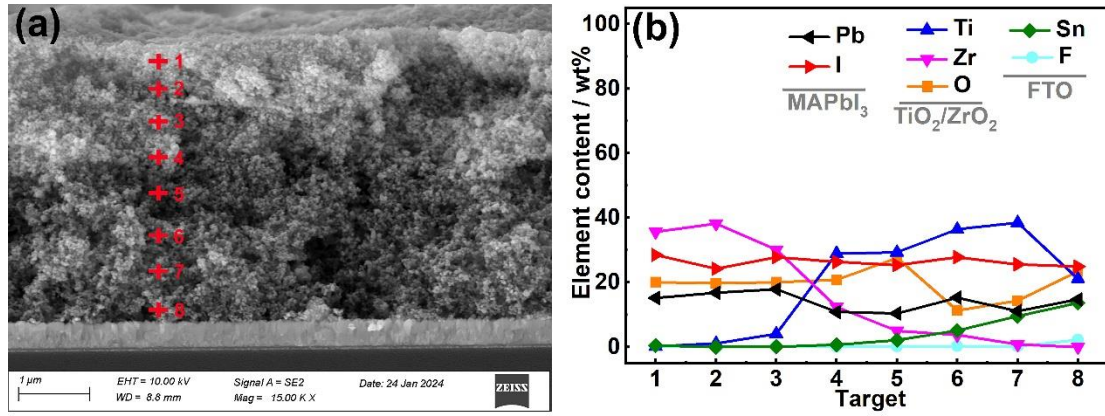


Fig. 5 Cross-sectional view of the TiO₂/ZrO₂ scaffold film with enhanced filling of MAPbI₃ material, showing the eight selected targets marked with red crosses for element distribution tracing (a). Comparative weight percent distribution of representative elements from MAPbI₃, TiO₂/ZrO₂, and FTO based on the targets from 1 to 8 (b).

When both the unenhanced-filling (Un-En) and enhanced-filling (En) scaffold films were assembled into PSCs, the typical photovoltaic performance is shown in Fig. 6. Both PSCs exhibit an open-circuit voltage (V_{oc}) of nearly 1.0 V, indicating that the P-N junction structure is intact and the voltage difference between the photoanode and counter electrode is consistent. However, the En PSC shows a short-circuit current density (J_{sc}) of 19.42 mA·cm⁻² and a fill factor (FF) of 57.51%, whereas the Un-En PSC shows a J_{sc} of 15.84 mA·cm⁻² and an FF of 16.47%. This improvement can be attributed to the enhanced perovskite filling in the scaffold layer, which both increases the light-harvesting capability of the cell and improves the perovskite/TiO₂ interface, facilitating carrier separation and transport while reducing the parallel resistance of the cell. Finally, the En PSC shows a conversion efficiency (η) of 10.60%, which represents a 375% improvement compared to the Un-En PSC. Furthermore, the batch stability of

the cell's photovoltaic performance was tested, as shown in Fig. 7. It can be observed that the mean values are $V_{oc} = 0.98$ V, $J_{sc} = 16.02$ mA·cm⁻², FF = 54.28%, and $\eta = 8.73\%$, demonstrating that enhancing the perovskite filling improves the stability of the cell structure, thereby achieving more stable performance. As a comparison, the same number of Un-En PSCs were also assembled, among which only 9 exhibited measurable conversion efficiency. The performance data of these efficient devices are presented in Figure S9. The poor filling state in the Un-En PSCs fails to provide stable pathways for charge transport, resulting in only a portion of the cells exhibiting low efficiency. The stability performance of the three parallel En PSCs are shown in Figure S8. It can be seen that the unencapsulated cells exhibit minimal performance degradation after being exposed to the ambient environment for 15 days.

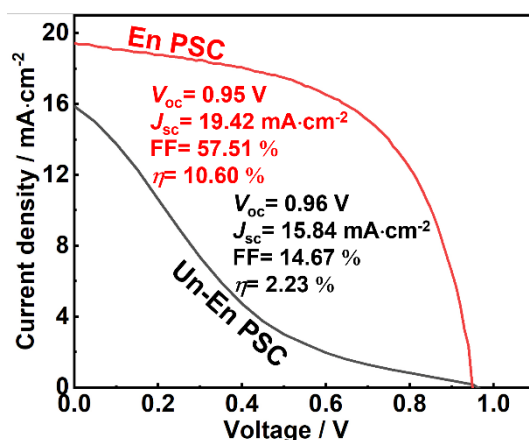


Fig. 6 Typical I - V results of the PSCs with the Un-En film (black line) and En film (red line)

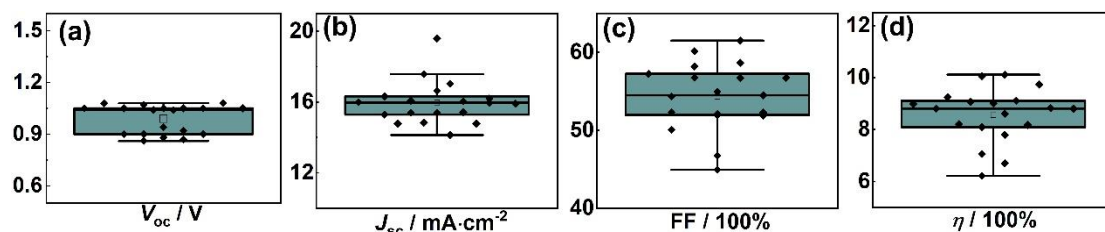


Fig. 7 Statistical results of the photovoltaic performance of the En PSCs: (a) V_{oc} , (b)

J_{sc} , (c) FF and (d) η

4. Conclusion

In this study, the filling results show that MAPbI₃ tends to aggregate in the upper area of the TiO₂/ZrO₂ scaffold film. To enhance the filling of the perovskite material, a physical filling dynamics model has been systematically proposed. This model divides the filling process into two stages: the initial infiltration of the perovskite precursor solution and the subsequent bottom-up crystallization of the perovskite precursor. During the experiment, PS microspheres are introduced to enhance porosity, and the temperature is kept low to restrain the evaporation of the solution. Additionally, bottom-up crystallization control is used to further improve perovskite incorporation into the scaffold layer. The EDS results show that the perovskite material is significantly filled within the inner part of the scaffold layer, and the photovoltaic performance confirms that increasing perovskite filling significantly enhances the conversion efficiency of the cells. In the future, enhancing capillary attraction and reducing evaporation will both contribute to the complete filling of perovskite materials into the active film.

Acknowledgements

National Natural Science Foundation of China (Grant No. 62204202), Natural Science Basic Research Program of Shaanxi Province (Grant No. 2024JC-YBMS-438), Youth Innovation Team of Colleges and Universities in Shaanxi Province, The Key Research and Development Program of Shaanxi Program (Grant No. 2023KXJ-172), 2024 Scientific Research Project of Shaanxi Institute of technology (Grant No. Gfy24-04)

Availability of Supporting Data

Several supporting information has been added as a single text.

Conflict of Interest

All the authors declare of no conflict of interest.

Reference

1. Green, M. A.; Dunlop, E. D.; Yoshita, M.; Kopidakis, N.; Bothe, K.; Siefert, G.; Hao, X., Solar cell efficiency tables (version 62). *Prog. Photovolt.: Res. Appl.* **2023**, *31*, 651-663.
2. Chen, B.; Yu, Z.; Onno, A.; Yu, Z.; Chen, S.; Wang, J.; Holman, Z. C.; Huang, J., Bifacial all-perovskite tandem solar cells. *Sci. Adv.* **2022**, *8*, eadd0377.
3. Ku, Z.; Rong, Y.; Xu, M.; Liu, T.; Han, H., Full Printable processed mesoscopic CH₃NH₃PbI₃/TiO₂ heterojunction solar cells with carbon counter electrode. *Sci. Rep.* **2013**, *3*, 3132.
4. Mei, A.; Li, X.; Liu, L.; Ku, Z.; Liu, T.; Rong, Y.; Xu, M.; Hu, M.; Chen, J.; Yang, Y.; Grätzel, M.; Han, H., A hole-conductor-free, fully printable mesoscopic perovskite solar cell with high stability. *Science* **2014**, *345*, 295-298.
5. Liu, L.; Mei, A.; Liu, T.; Jiang, P.; Sheng, Y.; Zhang, L.; Han, H., Fully printable mesoscopic perovskite solar cells with organic silane self-assembled monolayer. *J. Am. Chem. Soc.* **2015**, *137*, 1790-1793.
6. Hu, Y.; Si, S.; Mei, A.; Rong, Y.; Liu, H.; Li, X.; Han, H., Stable large-area (10 × 10 cm²) printable mesoscopic perovskite module exceeding 10% efficiency. *Solar RRL* **2017**, *1*, 1600019.
7. Fu, Z.; Xu, M.; Sheng, Y.; Yan, Z.; Meng, J.; Tong, C.; Li, D.; Wan, Z.; Ming, Y.; Mei, A.; Hu, Y.; Rong, Y.; Han, H., Encapsulation of printable mesoscopic

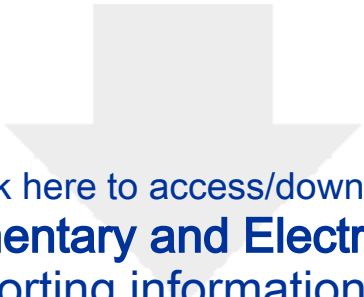
- perovskite solar cells enables high temperature and long-term outdoor stability. *Adv. Funct. Mater.* **2019**, *29*, 1809129.
8. Mei, A.; Sheng, Y.; Ming, Y.; Hu, Y.; Rong, Y.; Zhang, W.; Luo, S.; Na, G.; Tian, C.; Hou, X.; Xiong, Y.; Zhang, Z.; Liu, S.; Uchida, S.; Kim, T.-W.; Yuan, Y.; Zhang, L.; Zhou, Y.; Han, H., Stabilizing perovskite solar cells to IEC61215:2016 standards with over 9,000-h operational tracking. *Joule* **2020**, *4*, 2646-2660.
 9. Rong, Y.; Hu, Y.; Mei, A.; Tan, H.; Saidaminov, M. I.; Seok, S. I.; McGehee, M. D.; Sargent, E. H.; Han, H., Challenges for commercializing perovskite solar cells. *Science* **2018**, *361*, 5978.
 10. Ito, S.; Tsuji, R. Mesoscopic anodes and cathodes for printable perovskite solar cells. 2023, Chapter 4.
 11. Yao, Z.; Ning, Z. A breakthrough of printable mesoscopic perovskite solar cells. *Sci. Chi. Mater.* **2025**, *68*, 307-308.
 12. Cao, K.; Zuo, Z.; Cui, J.; Shen, Y.; Moehl, T.; Zakeeruddin, S. M.; Grätzel, M.; Wang, M., Efficient screen printed perovskite solar cells based on mesoscopic TiO₂/Al₂O₃/NiO/carbon architecture. *Nano Energ.* **2015**, *17*, 171-179.
 13. Duan, M.; Rong, Y.; Mei, A.; Hu, Y.; Sheng, Y.; Guan, Y.; Han, H., Efficient hole-conductor-free, fully printable mesoscopic perovskite solar cells with carbon electrode based on ultrathin graphite. *Carbon* **2017**, *120*, 71-76.
 14. Jiang, P.; Jones, T. W.; Duffy, N. W.; Anderson, K. F.; Bennett, R.; Grigore, M.; Marvig, P.; Xiong, Y.; Liu, T.; Sheng, Y.; Hong, L.; Hou, X.; Duan, M.; Hu, Y.; Rong, Y.; Wilson, G. J.; Han, H., Fully printable perovskite solar cells with highly-

- conductive, low-temperature, perovskite-compatible carbon electrode. *Carbon* **2018**, *129*, 830-836.
15. Xu, C.; Zhang, Z.; Hu, Y.; Sheng, Y.; Jiang, P.; Han, H.; Zhang, J., Printed hole-conductor-free mesoscopic perovskite solar cells with excellent long-term stability using PEAI as an additive. *J. Energ. Chem.* **2018**, *27*, 764-768.
16. Jeon, N. J.; Noh, J. H.; Kim, Y. C.; Yang, W. S.; Ryu, S.; Seok, S. I., Solvent engineering for high-performance inorganic–organic hybrid perovskite solar cells. *Nat. Mater.* **2014**, *13*, 897-903.
17. Wu, Y.; Islam, A.; Yang, X.; Qin, C.; Liu, J.; Zhang, K.; Peng, W.; Han, L., Retarding the crystallization of PbI₂ for highly reproducible planar-structured perovskite solar cells via sequential deposition. *Energ. Environ. Sci.* **2014**, *7*, 2934-2938.
18. Ahn, N.; Son, D.-Y.; Jang, I.-H.; Kang, S. M.; Choi, M.; Park, N.-G., Highly reproducible perovskite solar cells with average efficiency of 18.3% and best efficiency of 19.7% fabricated via lewis base adduct of lead(II) iodide. *J. Am. Chem. Soc.* **2015**, *137*, 8696-8699.
19. Hou, X.; Xu, M.; Tong, C.; Ji, W.; Fu, Z.; Wan, Z.; Hao, F.; Ming, Y.; Liu, S.; Hu, Y.; Han, H.; Rong, Y.; Yao, Y., High performance printable perovskite solar cells based on Cs_{0.1}FA_{0.9}PbI₃ in mesoporous scaffolds. *J. Power Sources* **2019**, *415*, 105-111.
20. Chen, J.; Rong, Y.; Mei, A.; Xiong, Y.; Liu, T.; Sheng, Y.; Jiang, P.; Hong, L.; Guan, Y.; Zhu, X.; Hou, X.; Duan, M.; Zhao, J.; Li, X.; Han, H., Hole-conductor-free

- dually printable mesoscopic solar cell with mixed-anion perovskite $\text{CH}_3\text{NH}_3\text{PbI}_{(3-x)}(\text{BF}_4)_x$. *Adv. Energ. Mater.* **2016**, *6*, 1502009.
21. Wang, Q.; Zhang, W.; Zhang, Z.; Liu, S.; Wu, J.; Guan, Y.; Mei, A.; Rong, Y.; Hu, Y.; Han, H., Crystallization control of ternary-cation perovskite absorber in triple-mesoscopic layer for efficient solar cells. *Adv. Energ. Mater.* **2020**, *10*, 1903092.
 22. Saliba, M.; Matsui, T.; Seo, J.-Y.; Domanski, K.; Correa-Baena, J.-P.; Nazeeruddin, M. K.; Zakeeruddin, S. M.; Tress, W.; Abate, A.; Hagfeldt, A.; Grätzel, M., Cesium-containing triple cation perovskite solar cells: improved stability, reproducibility and high efficiency. *Energ. Environ. Sci.* **2016**, *9*, 1989-1997.
 23. Saliba, M.; Matsui, T.; Domanski, K.; Seo, J.-Y.; Ummadisingu, A.; Zakeeruddin, S. M.; Correa-Baena, J.-P.; Tress, W. R.; Abate, A.; Hagfeldt, A.; Grätzel, M., Incorporation of rubidium cations into perovskite solar cells improves photovoltaic performance. *Science* **2016**, *354*, 206-209.
 24. Xiang, J.; Han, C.; Cheng, Y.; Gao, Q.; Hu, W.; Zhou, Y.; Mei, A.; Zhou, Y.; Han, H. Recent progress and advances of perovskite crystallization in carbon-based printable mesoscopic solar cells. *Adv. Mater.* **2025**, 2415405.
 25. Li, F.; Lin, F. R.; Jen, A. K. Y. Current state and future perspectives of printable organic and perovskite solar cells. *Adv. Mater.* **2024**, *36*, 2307161.
 26. Yang, H.; Zhao, J.; Zhou, T.; Zhang, H.; Zhang, W.; Zhang, J.; Hu, G.; Zhang, Y.; Liu, Q. Mesoporous TiO_2 electron transport materials derived from 2D Ti-MOFs for enhanced power conversion efficiency in Pprinted mesoscopic perovskite solar cells. *ACS Appl. Nano Mater.* **2023**, *6*, 16353-16361.

27. Worsley, C. A.; Dunlop, T. O.; Potts, S.-J.; Garcia-Rodriguez, R.; Bolton, R. S.; Davies, M. L.; Jewell, E.; Watson, T. M. Quantifying infiltration for quality control in printed mesoscopic perovskite solar cells: a microscopic perspective. *ACS Appl. Energ. Mater.* **2024**, *7*, 1938-1948.
28. Xiang, J.; Han, C.; Qi, J.; Cheng, Y.; Chen, K.; Ma, Y.; Xie, J.; Hu, Y.; Mei, A.; Zhou, Y. A Polymer defect passivator for efficient hole-conductor-free printable mesoscopic perovskite solar cells. *Adv. Funct. Mater.* **2023**, *33*, 2300473.
29. Wang, H.; Yang, F.; Li, X.; Zhang, P. Fully printed high-performance quasi-two-dimensional perovskite solar cells via multifunctional interfacial engineering. *Adv. Funct. Mater.* **2024**, *34*, 2312250.
30. Chen, J.; Xiong, Y.; Rong, Y.; Mei, A.; Sheng, Y.; Jiang, P.; Hu, Y.; Li, X.; Han, H., Solvent effect on the hole-conductor-free fully printable perovskite solar cells. *Nano Energ.* **2016**, *27*, 130-137.
31. Rong, Y.; Venkatesan, S.; Guo, R.; Wang, Y.; Bao, J.; Li, W.; Fan, Z.; Yao, Y., Critical kinetic control of non-stoichiometric intermediate phase transformation for efficient perovskite solar cells. *Nanoscale* **2016**, *8*, 12892-12899.
32. Jiang, Z.; Wang, B.; Zhang, W.; Yang, Z.; Li, M.; Ren, F.; Imran, T.; Sun, Z.; Zhang, S.; Zhang, Y.; Zhao, Z.; Liu, Z.; Chen, W., Solvent engineering towards scalable fabrication of high-quality perovskite films for efficient solar modules. *J. Energ. Chem.* **2023**, *80*, 689-710.
33. Bogachuk, D.; Girard, J.; Tilala, S.; Martineau, D.; Narbey, S.; Verma, A.; Hinsch, A.; Kohlstädt, M.; Wagner, L. Nanoarchitectonics in fully printed perovskite solar

- cells with carbon-based electrodes. *Nanoscale* **2023**, *15*, 3130-3134.
34. Gao L.; Yang G. J. Organic-inorganic halide perovskites: from crystallization of polycrystalline films to solar cell applications *Solar RRL* **2019**, *12*, 1900200.
 35. Ding B.; Li Y.; Huang S. Y.; Chu Q. Q.; Li C. X.; Li C. J.; Yang G. J.; Material nucleation/growth competition tuning towards highly reproducible planar perovskite solar cells with efficiency exceeding 20% *J. Mater. Chem. A* **2017**, *5*, 6840-6848.
 36. Ding B.; Gao L. L.; Liang L. S.; Chu Q. Q.; Song X. X.; Li Y.; Yang G. J.; Fan B.; Wang M. K.; Li C. X.; Li C. J. Facile and scalable fabrication of highly efficient lead iodide perovskite thin-film solar cells in air using gas pump method, *ACS Appl. Mater. Interf.* **2016**, *8*, 20067-20073.
 37. Zhao, Y.; Zhu, K., Solution chemistry engineering toward high-efficiency perovskite solar cells. *J. Phys. Chem. Lett.* **2014**, *5*, 4175-4186.
 38. Han, H.; Bach, U.; Cheng, Y.-B.; Caruso, R. A.; MacRae, C., A design for monolithic all-solid-state dye-sensitized solar cells with a platinized carbon counterelectrode. *Appl. Phys. Lett.* **2009**, *94*, 103102.
 39. Heo, J. H.; Song, D. H.; Im, S. H., Planar CH₃NH₃PbBr₃ hybrid solar cells with 10.4% power conversion efficiency, fabricated by controlled crystallization in the spin-coating process. *Adv. Mater.* **2014**, *26*, 8179-8183.
 40. Li, Y.; Li, X.; Chu, Q.; Dong, H.; Yao, J.; Zhou, Y.; Yang, G., Tuning nucleation sites to enable monolayer perovskite films for highly efficient perovskite solar cells. *Coatings* **2018**, *8*, 408.



[Click here to access/download](#)
Supplementary and Electronic files
Supporting information.docx

